Fall 12-10-2022

FABRICATION, CHARACTERIZATION, AND SIMULATION OF GRAPHENE-COPPER ELECTRICAL CONDUCTORS

Raju Prasad Ghimire
University of New Mexico - Main Campus

Recommended Citation

Ghimire, Raju Prasad. "FABRICATION, CHARACTERIZATION, AND SIMULATION OF GRAPHENE-COPPER ELECTRICAL CONDUCTORS." (2022). https://digitalrepository.unm.edu/nsms_etds/76

Raju Prasad Ghimire

Candidate

Nanoscience and Microsystems

Department

This dissertation is approved, and it is acceptable in quality and form for publication:

Approved by the Dissertation Committee:

Yu-Lin Shen, Ph.D., Chairperson

Sang M. Han, Ph.D.

Ivana Gonzales, Ph.D.

Mehran Tehrani, Ph.D.

FABRICATION, CHARACTERIZATION, AND SIMULATION OF GRAPHENE-COPPER ELECTRICAL CONDUCTORS

by

RAJU PRASAD GHIMIRE

B.SC., TRIBHUVAN UNIVERSITY, NEPAL (2007)

M.SC., TRIBHUVAN UNIVERSITY, NEPAL (2012)

M.S., SOUTH DAKOTA STATE UNIVERITY, USA (2018)

DISSERTATION

Submitted in Partial Fulfillment of the

Requirements for the Degree of

Doctor of Philosophy in Engineering

The University of New Mexico

Albuquerque, New Mexico

DECEMBER 2021

DEDICATIONS

This dissertation is dedicated to my parents, family members, friends, and my wonderful wife, Bhawana, who were patient and supportive of me over the last three years. And to my baby, Zoya, who I trust will benefit from this work.

ACKNOWLEDGEMENTS

I kindly and emphatically acknowledge Dr. Mehran Tehrani for his support, time, and dedication. Not only was he my graduate advisor, but he was also a guardian without whom I could not have achieved this feat. It was three years ago when he decided to supervise my graduate work, as a result of which I have been fledged to become a competent researcher. His guidance, encouragement, insights, and relentless support, along with much-needed harsh criticisms, were indispensable for completing my research work. Moreover, I would like to acknowledge Dr. Tehrani for providing me with the opportunity to work in his lab at The University of Texas at Austin as a visiting research student. My sincere gratitude extends to Dr. Yu-Lin Shen for kindly accepting the position of my committee chair in place of Dr. Tehrani upon his relocation to UT Austin.

I would also like to extend my gratitude to Dr. Ivana Gonzales for her contribution to this dissertation, atomistic simulation of multi-layered graphene copper films. My work would not have been complete without her results and support. I can’t forget her swift and prompt responses to every question and email and her availability for discussions.

This dissertation would not have been possible without the help of my group members, technical staff, and scientists, who helped me whenever needed. My special thanks go to Pouria Khanbolouki, Moein Mohammadi, and Pratik Koirala for their time and expertise in obtaining data from various characterization techniques and interpreting them scientifically.

I would like to acknowledge the support and opportunity provided by the American Physical Society for getting involved in the science policy advocacy. It improved my leadership skills and helped me translate my dream into reality, which was to leave an impact towards international students living in the United States of America.

Finally, I would like to express my sincere appreciation to Dr. Sang M. Han for agreeing to serve as a committee member and his tremendous support and guidance while writing this dissertation. Additionally, I cannot overlook the logistic support from the program's graduate coordinator, Linda Stewart. I owe you all a lot!

Fabrication, Characterization, and Simulation of Graphene-Copper Electrical Conductors

By:

Raju Prasad Ghimire

B.SC., Tribhuvan University, Nepal (2007)

M.SC., Tribhuvan University, Nepal (2012)

M.S., South Dakota State University, USA (2018)

Ph.D., The University of New Mexico, USA (2021)

ABSTRACT

The addition of nanocarbons to copper (Cu), specifically in the form of graphene (GN), has been shown to enhance copper's properties. GN-Cu nanocomposites can potentially achieve higher electrical, mechanical, and thermal properties compared with copper. These characteristics make GN-Cu materials interesting for several applications including but not limited to interconnects, high voltage lines, and rotating machines. Copper's microstructure and nanoscale interfacial phenomena between the GN and Cu control charge conduction in GN-Cu materials. In this work, we investigated the possibilities of conductivity enhancement in multi-layered GN-Cu composites both theoretically (classical, quantum, and atomistic models) and experimentally.

Additionally, our work elucidates possible errors in electrical conductivity measurements of thin GN-Cu films. GN-Cu samples were prepared by the processing of chemical vapor deposition (CVD) GN on Cu samples using spark plasma sintering (SPS) or hot isostatic pressing (HIP). Structure-property relationships, measured over a wide temperature range, revealed conduction mechanisms in these materials. This dissertation also investigates the high electrical current processing of copper-carbon melt, namely the Covetic processing.

Table of Contents

List of Figures

List of Tables

Chapter 1. Introduction

1.1 Motivation

Room temperature electrical conductors that outperform copper's (Cu) electrical conductivity or aluminum's (Al) conductivity per weight are highly desired for power transmission, communications, electronics, and electric machines by many industries [1]. Advanced electrical conductors, also called ultra-conductors, offer unique and exceptional physical properties by means of utilizing nanocarbons, mostly carbon nanotubes (CNT) and graphene (GN), alloying, or controlling grain size and texture. Advanced electrical conductors can revolutionize our lives, resulting in savings of energy and money and facilitating a transition to an electric mobility future.

Advanced electrical conductors can be categorized into three groups based on the host conductor material and additives: pure metal-based, nanocarbon-based, and metal-carbon conductors. Pure metal-based ones are fabricated by purification, single crystal growth, or alloying with other metal elements. Carbon allotropes such as graphite, GN, and CNT constitute the basis for both nanocarbon-based and metal-carbon electrical conductors. Nanocarbon-based conductors are mostly comprised of CNT or GN with small quantities of other elements and compounds for improving their conductivity. Metal-carbon conductors are metals that contain a small loading of CNT, GN, or occasionally other carbon allotropes. It seems that the performance of pure metal-based conductors is already saturated, and researchers are mostly focused on the nanocarbon-based and metal-carbon-based advanced conductors because of their potential for light-weighting and multi-functionality.

Carbon nanotube-based conductors have been rigorously researched for over 20 years now,[2] but their promise of surpassing copper's electrical conductivity has not yet been realized [3]. Occasionally, doped-CNT and Cu-CNT conductors that outperform copper on a weight basis at room temperature are reported. Graphene has a relatively similar structure to CNTs, yet its interaction with Cu is different. The addition of graphene to Cu affect copper's micro-structure and conductivity [4-7]. Most notably, a very small loading of graphene (<0.001%) is required to cause measurable improvements in copper's conductivity [8, 9]. This dissertation, therefore, focuses mostly on GN-based conductors and sets out to reveal the fundamentals of their processing, materials science, and measurements.

1.2 Dissertation Overview

This dissertation investigates the materials science (processing-structure-property relationships) of nanocarbon-copper conductors from theoretical and experimental perspectives. It also elucidates the importance of error analysis in electrical conductivity measurements of advanced electrical conductors.

In chapter 2, the electrical conductivity of graphene copper multi-layered structures is modeled by combining a classical conductivity model with quantum calculations of charge transfer between copper and graphene. This chapter discusses the feasibility of ultra-conductivity in graphene copper multi-layered structures.

Graphene copper multi-layered electrical conductors, processed at high temperatures and pressures, are investigated both experimentally and numerically in Chapter 3. This chapter comprises room and elevated temperature electrical conductivity measurements, including error analysis for conductivity measurements of annealed metal thin films. Micro-structure of samples is correlated to their properties. Finally, atomistic simulations are used to explain the electronic hybridization of copper and graphene at their interface.

Chapter 4 scrutinizes the effect of hot isostatic pressing (HIP) on electrical properties of the various graphene-coated copper samples (foil, foam, and wire). Electrical properties, including electrical conductivity, maximum current rating (ampacity), temperature coefficient of resistance (TCR) are measured and correlated with samples' structure, determined via X-ray diffraction and microscopy.

Copper carbon interfaces achieved under covetic processing, application of high currents above copper's melting temperature, are investigated in Chapter 5. Multi-layered structures of copper and different carbon sources treated under high currents didn't show signs of hybrid materials formation, as claimed by others in covetic processing. The electrical properties at the interface between copper and carbon layers are investigated using conductive atomic force microscopy (c-AFM).

Lastly, Chapter 6 summarizes this dissertation's major conclusions and recommendations for future work that can be built off the results found here.

Chapter 2. Classical Modeling of Multi-Layered Graphene Copper Ultra-Conductors

Abstract: Graphene-copper multi-layered films, containing less than 100 ppm graphene, have recently demonstrated electrical properties surpassing copper's by as much as 117%. In this study, the electrical conductivity of such multi-layered ultra-conductors is calculated using a classical model. Fermi level shift and charge transfer due to the work function difference between graphene and copper were calculated. The conductance of the multi-layered conductor is then calculated by adding the conductance of the individual constituents. Several scenarios are considered that justify a ~17% improvement in copper's conductivity: either a carrier mobility enhancement of ~17% in copper or an extremely high mobility for the sandwiched graphene, i.e., two orders of magnitude higher than the mobility of freestanding graphene. This paper discusses the limitations of classical electrical conductivity models and sheds light on the underlying mechanisms responsible for the improved electrical conductivity of the graphene-copper ultra-conductors.

2.1 Introduction

Electrical conductors that outperform copper (Cu) are highly desired for power transmission and generation, communications, electronics, and electric machines [10]. Graphene offers excellent intrinsic electrical properties and is, therefore, considered a promising additive for improving the electrical properties of metals. Recently, there has been a report of ultra-conductivity, 117% conductivity of International Annealed Copper Standard (IACS), in a multi-layered sample made by hot pressing multiple copper foils, each covered with a few layers of chemically grown graphene [11]. The 117% improvement is attributed to copper's enhanced conductivity (13%), presumably from the processing itself, and graphene's conduction of electrons transferred from copper (4%). It is worth noting that the graphene's loading in these samples was less than 0.01%. Other studies also suggest enhanced electrical conductivity and temperature coefficient of resistance in metal-graphene nanocomposites compared with the pure metallic conductors [11-16].

Interfacial charge transfers are ubiquitous in electronic and optoelectronic devices made from graphene. Charge transfer plays a crucial role in determining the electrical properties of graphene-metal conductors. Suppose enough charges readily transfer from the metal to graphene. In that case, the hybrid metal-graphene material can potentially combine the ballistic electron transport in graphene with the abundant electron density of the metal, resulting in superior electrical conductivities [1]. While graphene can potentially enhance the electrical conductivity of metals, other additives may only scatter electrons, reducing the overall conductivity of the host metal.

When two materials of different work function (Φ) come in contact, electrons are transferred between them, aligning their Fermi levels. Electron transfer, therefore, alters the electronic properties of both contacting materials. Metal graphene junctions behave differently than metal-metal or metal-semiconductor ones [17-21]. For a free-standing graphene touching metal pads, the charge transfer aligns the Fermi levels of both graphene and metal [22]. The Fermi level of graphene is brought under the metal contacts from the charge neutrality point. In contrast, the Fermi level of the region far from the contacts remains unchanged at the neutrality point [22].

The electron transfer between a metal and graphene touching one another depends on their separation distance (d-spacing), determined by their work functions and bonding type. The metal-graphene bonding type is broadly classified into two main categories of physisorption (PH) and chemisorption (CH) [23-26]. Graphene's electronic structure is almost unaltered in physisorption compared to free-standing graphene, which only occurs when graphene is exposed to weakly interacting metals. On the contrary, the graphene's electronic structure is intensely perturbed due to the strong hybridization between metal$-d$ and carbon$-\pi$ orbitals in chemisorption, occurring with strongly interacting metals [27]. Figure 1 clearly shows the approximate *d*-spacings values for physisorption (~0.33) and chemisorption (~0.21) bonding types.

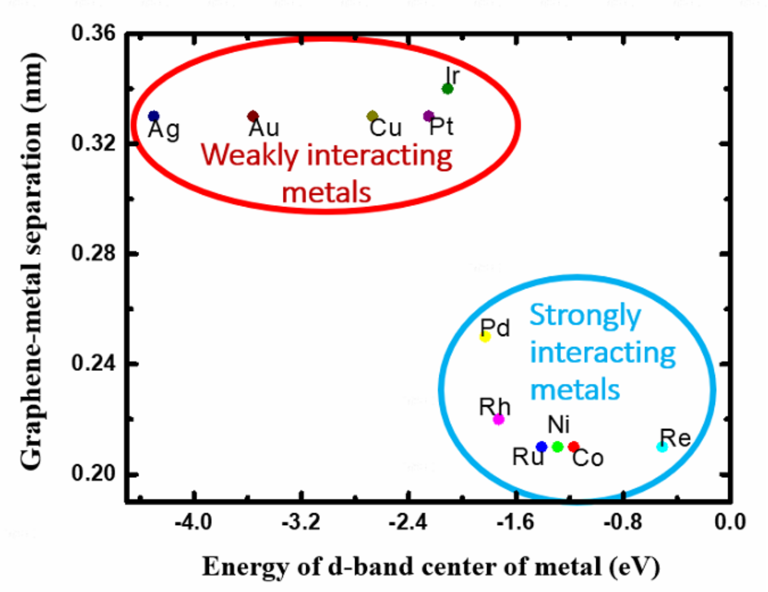

Figure 1: The relationship between the graphene-metal separation and the energy of d-band center of different transition metals [28].

Figure 2 shows the reported work function values for both graphene and copper [29-31]. It is assumed here that the graphene's work function is always smaller than that of the copper, representing the majority of the experimental measurements [32-37]. The average work function value of graphene (~4.48 eV) is smaller than that of copper (~4.6 eV). The number of electrons that can transfer from copper to graphene can be estimated based on their work function and *d*-spacing.

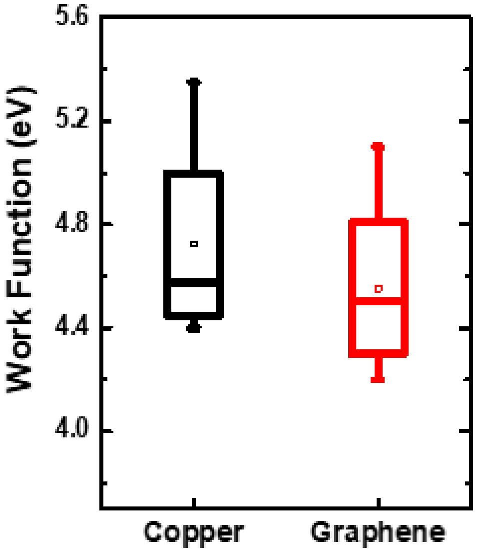

Figure 2: Ranges of work function values of copper and graphene. Plotted data is based on [29-31].

Experimentally measured electrical conductivities of individual copper and graphene, based on their electron densities and mobility, are consistent with theoretical predictions [38-44]. Electrical conductivity of metals can be enhanced with the addition of graphene [11, 13, 39, 45-48]. It is, however, not clear whether this improvement is due to the graphene's ultrahigh electron mobility, interfacial phenomena, reduction of metal's defect density, or their combination. There has been several studies on metal-graphene electronic interactions using atomistic models [49-54]. The superior electron mobility of graphene explains the enhanced electrical conductivity of graphene-copper systems even at high electron densities [11, 54]. The electrical conduction in graphene-copper composites is not well understood. In this paper, possible ranges for the electron density and corresponding electron mobility in graphene or graphene-copper interfaces are considered, using classical conduction models, to explain the ultrahigh electrical conductivity of graphene-copper multi-layers. This paper also discusses the limitations of classical models and sheds light on the mechanisms responsible for the improved electrical conductivity in graphene-copper composites.

2.2 Modeling

The general conductivity and the Drude models were adopted to calculate the electrical conductivity of the graphene-copper multi-layered structures. Reported literature values for the work functions and d-spacing for copper, graphene, and graphene on copper were used for the calculations. Figure 3 depicts the structure of the graphene unit cell, showing that it has two atoms per unit cell, and the area of each unit cell (ABCD in Figure 3) is nearly $5.18\,\text{Å}^2$. The electron density of graphene ranges from 10^{10} to 10^{14} cm^{-2} according to the literature [55-58]; measured for free-standing graphene and graphene on different substrates. Graphene's electron density depends on its substrate and chemical groups attached to it [38, 57, 59]. Copper's electron density was adjusted from a 3-dimensional foil to a 2-dimensional copper layer to match graphene's 2-dimensional electron density and vice versa.

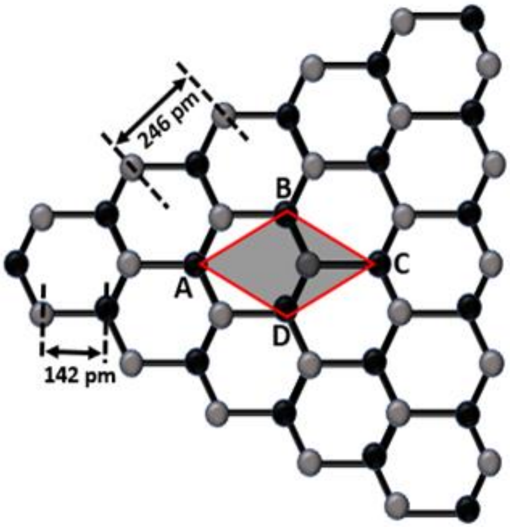

Figure 3: Representation of Graphene's unit cell.

Several steps are carried out to calculate the electrical conductivity of a multi-layered graphene-copper conductor. First, the Fermi level shift at different d-spacing of the graphene-copper interface was calculated. Second, the number of electrons that can possibly transfer from copper to graphene was estimated. Third, the total number of electrons transferred over a 1 cm^2 of graphene was calculated. Forth, the total electron densities, after the electron transfer, for both copper and graphene were calculated. Next, the conductance of each material was calculated and added to obtain the total conductance. Finally, possible scenarios justifying ultra-conductivity in the graphene-copper system are discussed.

2.2.1 Fermi level shift and charge transfer calculations

A microscopic model developed by Giovannetti et al. and Khomyakov et al. [23, 60] was used to calculate the Fermi level shift and the number of electrons transferred between copper and graphene. Figure 4 shows the Fermi level shift, work function, d-spacing, and developed potential at the graphene-copper interface. The work function of the graphene-copper system can be defined as:

$$W_{Gr+Cu} = W_{Cu} - \Delta V(d) \tag{1}$$

where W_{Gr+Cu} is the work function of the graphene-copper system, W_{Cu} is the copper's work function, $\Delta V(d)$ is the potential step generated by the interface dipole layer, and d is the d-spacing. The Fermi level shift in graphene can be written as:

$$\Delta E_F = W_{Gr+Cu} - W_{Gr} \tag{2}$$

where ΔE_F is graphene's Fermi level shift and W_{Gr} is graphene's work function.

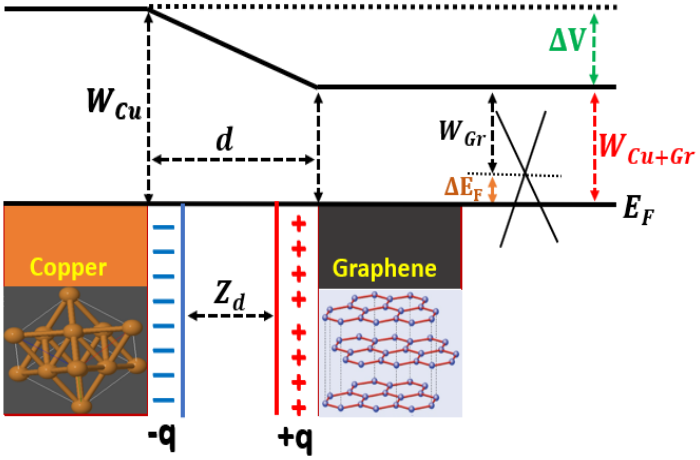

Figure 4: Energy band diagram of the copper graphene system.

Combining (1) and (2), gives:

$$\varDelta E_F = W_{Cu} - W_{Gr} - \varDelta V(d) \quad (3)$$

The potential step generated by the interface dipole layer can be further written as:

$$\varDelta V(d) = \varDelta_{tr}(d) + \varDelta_c(d) \quad (4)$$

where $\varDelta_{tr}(d)$ is the non-interacting charge transfer contribution due to the work function difference between copper and graphene and $\varDelta_c(d)$ is the short-range interaction due to graphene copper chemical interaction. The charge transfer can be written as:

$$\Delta_{tr}(d) = \alpha N(d) Z_d \quad (5)$$

where $\alpha = \frac{e^2}{\epsilon_o A} = 34.93\ \frac{eV}{\text{Å}}$; $A = 5.18\ \text{Å}^2$ = graphene area, *N(d)* = Number of electrons (per unit cell) transferred from either graphene to copper (+ve) or copper to graphene (-ve), $Z_d = d - d_0$ is the effective distance between the charge sheets on graphene and copper, as shown in Figure 4. The short-range interaction can be expressed in terms of the d-spacing between the metal and graphene as[23]:

$$\Delta_c(d) = e^{-kd}(\alpha_o + \alpha_1 d + \alpha_2 d^2)$$
(6)

where $k = 1.6443\ \frac{1}{\text{Å}}$, $\alpha_o = -2048.56\ eV$, $\alpha_1 = 1363.87\ \frac{eV}{\text{Å}}$, $\alpha_2 = -205.737\ \frac{eV}{\text{Å}^2}$ [23, 60]

Combining equations (1) through (6), gives:

$$\Delta E_F(d) = \frac{\pm\sqrt{1+2\alpha D_o(d-d_o)|W_{Cu}-W_{Gr}-\Delta_c(d)|}-1}{\alpha D_o(d-d_o)}$$
(7)

where $D_0 = 0.09\ eV^2$ per unit cell [23].

Finally, the number of electrons transferred per unit cell of graphene is calculated as:

$$N(d) = \pm\frac{D_o \Delta E_F^2}{2}$$
(8)

2.2.2 *Drude model and DC conductivity*

High-frequency AC conductivity of monolayer graphene follows a Drude form $\sigma_\omega = \left[\frac{iD}{\pi(\omega+i\Gamma)}\right]$, where ω is the frequency and Γ is the scattering rate. Pre-factor D is known as the Drude factor, defined as $D = (\frac{v_f e^2}{\hbar})\sqrt{\pi \mid n \mid}$, when electron-electron interactions are neglected and $v_f = 1.1 \times 10^6\ \frac{m}{s}$ being the Fermi velocity and $|n|$ is the carrier density [61]. Since the focus of this study is the DC electrical conductivity, the Drude model is modified as follows:

$$\sigma_{dc} = \left(\frac{D}{\pi\Gamma}\right)$$
(9)

$$D = \left[\left(\frac{v_f e^2}{\hbar}\right)\sqrt{\pi \mid n \mid}\right]$$
(10)

$$\Gamma = \left[\frac{ev_f^2}{\mu E_f}\right]$$

(11)

$$E_f = [\hbar v_f \sqrt{\pi \mid n \mid}]$$

(12)

where v_f = Fermi velocity, n and μ are carrier density and mobility, respectively, and E_f = Fermi energy. Combining equations (9) to (12), graphene's DC conductivity can be written as, $\sigma_{dc} = ne\mu$. The DC conductivity equation for graphene turns out to be identical to that of metals.

2.2.3 Conductance and conductivity calculations

The total conductance of the graphene-copper multi-layered material can be written as:

$$G_{total} = N_{Cu} \times G_{Cu} + N_{Gr} \times G_{Gr}$$

(13)

where G_{cu}, G_{Gr}, and G_{total} are the conductance's of copper, graphene, and the graphene-copper structure, respectively, and N_{Cu} and N_{Gr} are the number of copper and graphene/interface layers. The conductance equation can be further simplified considering that copper donates electrons and graphene accepts them:

$$G_{Cu} = \sigma_{Cu} \times t_{Cu} = (ne\mu)_{Cu} \times t_{Cu} = (n_{Cu} - \Delta n) \times e \times \mu_{Cu} \times t_{Cu}$$

(14)

$$G_{Gr} = \sigma_{Gr} = (ne\mu)_{Gr} = (n_{Gr} + \Delta n) \times e \times \mu_{Gr}$$

(15)

Finally, the total conductivity is calculated as:

$$\sigma_{total} = \frac{G_{total}}{t_{total}} \tag{16}$$

The graphene-copper multi-layered structure that is studied here is based on the study by Cao Mu et al. [11], consisting of consolidated stacks of graphene-covered copper foils. In the model, the stacking has a repeating structure of single graphene layers deposited on both side of 25 μm copper foils: two graphene layers are sandwiched at each interface. Figure 5 depicts the multi-layered and unit structure of such a system. Considering the graphene copper d-spacing (~0.221 nm), the thickness of each copper foil (25 μm), and each graphene layer (0.335 nm) results in a total unit structure thickness of ~ 25.001112 μm.

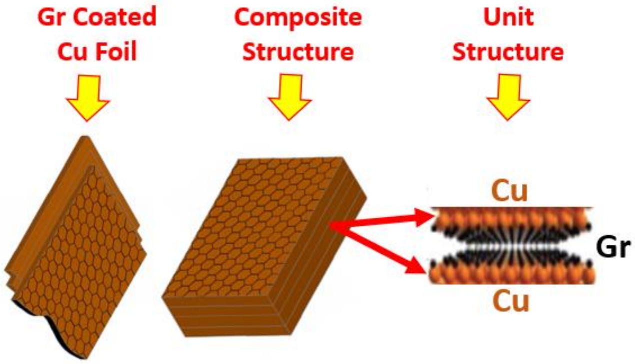

Figure 5: Foil, multi-layered, and unit structure for the copper-graphene conductor.

2.3 Results and Discussions

Electron transfer in metal-graphene systems depends on the work function difference and d-spacing, as described in equation (7), between the graphene and the metal. Electron transfer results in the formation of an interface dipole layer and an accompanying potential step ($\Delta V(d)$), and its size determines the smoothness of electron transfer. A potential step is a combination of non-interacting charge transfer ($\Delta_{tr}(d)$), due to work function difference, and short-range interaction ($\Delta_c(d)$), due to metal graphene chemical interaction.

The possible range of electrons transferred from metal to graphene can be calculated by varying the work function or the d-spacing. Electron transfer is dominated by d-spacing when its value is less than 4 Å and dominated by work function when d-spacing is more than 4 Å [23, 60, 62]. In the case of the graphene-copper system, the d-spacing is less than 4 Å [60, 62]. Therefore, the number of electrons transferred is estimated by varying the d-spacing. In this work, the d-spacing of the copper-graphene system was varied from 0.221 nm to 0.37 nm to cover the possible range of electron transfer. It should be noted that more realistic simulations, such as atomistic models, may calculate much higher electron transfer for a given d-spacing.

Table 1 illustrates the possible values of the Fermi level shift and the number of electrons transferred, from copper to graphene, at three different d-spacing values. As the effective distance between graphene and copper increases, the number of electrons transferred is reduced and vice versa. The calculation in Table 1 shows that more electrons transfer with smaller d-spacings. The number of electrons transferred from copper to graphene $(N) = N_t \times N_d$, where $N_t =$ number of a primitive unit cell of graphene in a 1 cm^2 area and $N_d =$ number of electrons transferred from the copper to graphene per unit cell. The approximate area of the primitive graphene unit cell is $\sim 5.18\,\text{Å}^2$. The number of primitive graphene unit cells in a 1 cm^2 area can be obtained as $(N_t) = \frac{1\ \text{cm}^2}{\text{Area of primitive unit cell}} = \frac{1\times10^{16}\ \text{Å}^2}{5.18\ \text{Å}^2} = 1.93 \times 10^{15}$.

Estimation of minimum and maximum number of electrons transferred from copper to graphene in a 1 cm^2 sample area was performed using the values obtained in Table 1 associated with two extremes of the d-spacings considered. The number of electrons transferred for a 2.21 Å d-spacing is similar to density functional theory calculations [11] which shows that a primitive cell of bilayer graphene (containing four carbon atoms) obtains an average of ~0.24 electrons from neighboring copper atoms.

Table 1: Fermi level shift and number of electrons transferred from copper to a unit cell of graphene with respect to graphene-copper d-spacing

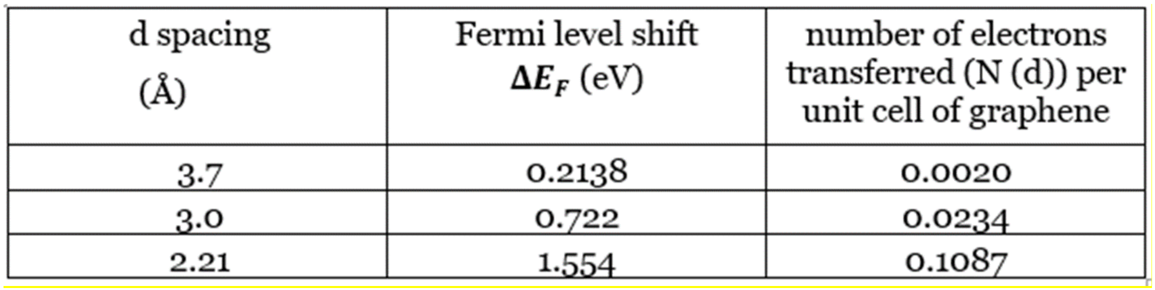

d spacing (Å)	Fermi level shift ΔE_F (eV)	number of electrons transferred (N (d)) per unit cell of graphene
3.7	0.2138	0.0020
3.0	0.722	0.0234
2.21	1.554	0.1087

Table 2 shows the ranges of electron densities in graphene before and after the electron transfer from copper. Copper offers a large electron density ($\sim 8.49 \times 10^{22}$ e cm^{-3}) and can donate a considerable amount to graphene without compromising its own conductivity. Electron transfer, in this case, is limited mainly by work function and d-spacing. The estimated electron density in Table 2 shows the minimum ($\sim 3.86 \times 10^{12}$ e cm^{-2}) and maximum ($\sim 3.09 \times 10^{14}$ e cm^{-2}) electron densities graphene achieves after accepting electrons from copper. The final graphene's electron density is within the ranges of graphene's electron densities found in the literature [55-58]. The new electron densities might alter the electron mobility in graphene, but the electron mobility in copper is not expected to change.

Table 2: Copper and graphene's initial and potential final electron densities after electron transfer [55-58].

	Initial electron densities (e cm^{-2})		Electron transfer from copper to graphene (e cm^{-2})	Final electron densities (e cm^{-2})	
	Graphene [55-58]	Copper		Graphene	Copper
Minimum	10^{10}	1.93×10^{15}	3.86×10^{12}	3.86×10^{12}	1.93×10^{15}
Maximum	10^{14}	1.93×10^{15}	2.09×10^{14}	3.09×10^{14}	1.72×10^{15}

It is well established that the copper's electron mobility is ~ 42.78 $\mathrm{cm^2/(V.S)}$ for an electron density of $\sim 8.49 \times 10^{22}$ $\mathrm{e\ cm^{-3}}$, achieving an electrical conductivity of 58.1 MS/m (100% of IACS). The electrical conductivity of single crystal copper treated at high temperatures and pressures has been reported to be as high as 113% IACS [63, 64]. While copper's electron density is unchanged, the electron mobility in single-crystal copper should have increased by 13%. The calculated electron mobility of the treated single crystal copper is, therefore, $\sim 48.37\ \mathrm{cm^2/(V.S)}$. On the other hand, graphene can possess various electron mobilities corresponding to different electron densities, and it seems that ultrahigh electron mobilities in graphene are possible only for relatively low electron densities [55-58]. For instance, carrier mobility values of $\sim 2 \times 10^5\ \mathrm{cm^2/(V.S)}$ and $\sim 1 \times 10^7\ \mathrm{cm^2/(V.S)}$ were measured at carrier densities of $\sim 3 \times 10^9\ e\ cm^{-2}$ for single layer free-standing graphene and graphene on a graphite substrate, respectively [65, 66]. Researchers are trying to overcome this trade-off by incorporating graphene into different structures. For example, the electron mobility of van der Waals heterostructures formed by graphene and hexagonal boron nitride (hBN) outperforms that of all known materials. The graphene heterostructure formed by tungsten diselenide (WSe_2)/graphene/hBN structure [67] exhibits an electron mobility of $\sim 350{,}000\ cm^2/(V.S)$while having an electron density of $2 \times 10^{12}\ \mathrm{e\ cm^{-2}}$. Intuitively, a higher electron mobility even at higher electron densities might be possible when graphene interacts via van der Waals interactions with other materials, such as copper.

Table 3 summarizes possible conductivity values for the multi-layered copper-graphene system at different electron densities and mobilities, also depicted in Figure 6. It is safe to assume that that the copper electron density does not change significantly after electron transfer. For the multi-layered structure to achieve a ~117% IACS, the calculations suggest that the graphene or the interface mobility should be in the order of $\sim 10^5\ \mathrm{cm^2/(V.S)}$ even at higher electron densities ($\sim 10^{14}\ \mathrm{e\ cm^{-2}}$). Such unexpectedly high mobility and electron density in graphene is also claimed by others [11]. Despite these claims, the electron densities and mobilities are far above the upper limits predicted by theory for pristine graphene [68, 69].

Table 3: Possible electron densities and mobilities of copper and graphene in the multilayered system.

	Electron	Case-I (100% IACS)	Case-II (113% IACS)	Case-III (117% IACS)
Copper	Density (n) ($\mathrm{e\ cm^{-3}}$)	8.4×10^{22}	8.4×10^{22}	8.4×10^{22}
	Mobility (μ) ($\mathrm{cm^2/(V.S)}$)	42.92	48.37	48.37
Graphene	Density (n) ($\mathrm{e\ cm^{-2}}$)	3.86×10^{12}	3.86×10^{12}	3.09×10^{14}
	Mobility (μ) ($\mathrm{cm^2/(V.S)}$)	$0 - 1 \times 10^{8}$	$0 - 1 \times 10^{8}$	8.4×10^{5}

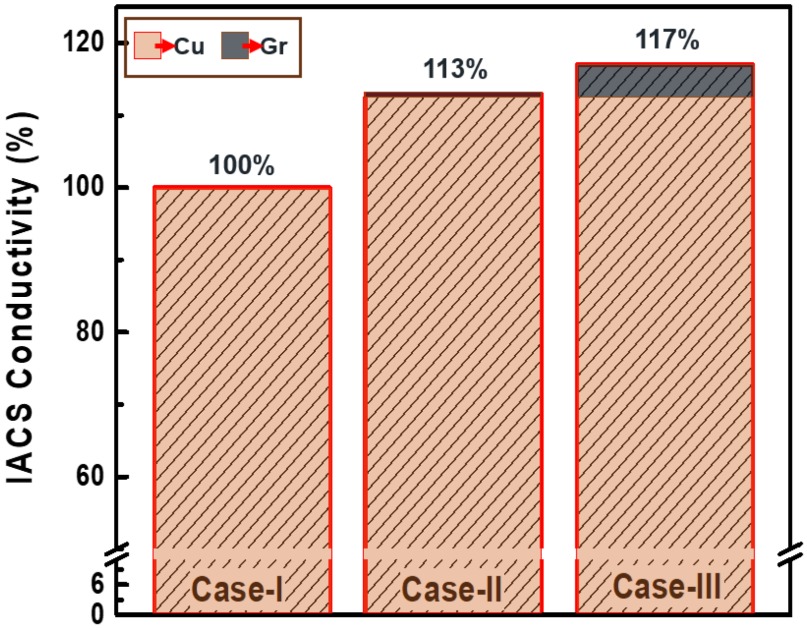

Figure 6: Illustration of possible electrical conductivity contributions in multi-layered systems from both copper and graphene.

As mentioned earlier, single crystal copper reaches 110% IACS, and its post-processing can further improve its electrical conductivity to 113% IACS [63, 64]. Considering the electrical conductivity of a graphene-copper multi-layered structure at ~117% IACS and assuming that the copper achieves its maximum reported conductivity (~113% of IACS), graphene would be responsible for the remaining improvement of about 4% IACS, as shown in Figure 6. In this case, the graphene electron mobility should be in the order of $10^5 \mathrm{cm}^2/(\mathrm{V.S})$ for an electron density of around 10^{14} e cm^{-2}. These values are not in an acceptable range for graphene. Copper crystal changes its orientation to (111) during graphene growth and consolidation into multi-layered films [11]. The copper (111) facet also has a hexagonal crystal structure, and atomic spacings of copper ($Cu_{111} = 2.56$ Å) and graphene ($Gr = 2.46$ Å) are a close match. Graphene is sandwiched between two copper foils in the modeled samples, and the (111) texture and sandwich structure might be in favor of having higher electron mobilities even at higher electron densities for graphene. Finally, new interfacial phenomena can happen at interfaces. To the best of the authors' knowledge, there is no reported literature on ultrahigh electron mobility at higher electron density in graphene devices. However, the formation of a new structure at the copper graphene interface may result in a higher electron mobility even at a high electron density.

2.4 Conclusions

The combined quantum-classical calculations show that graphene sandwiched between copper layers can accept electrons from copper and contribute to the overall conductivity if it can achieve mobilities that are higher than freestanding graphene. This means that graphene or the interface between graphene and copper should achieve ultrahigh electron mobility even at high electron densities.

2.5 Acknowledgements

The authors acknowledge the support by the Office of Naval Research (ONR) under Grant No. N00014-18-1-2441.

Chapter 3. Fabrication, Characterization, and Atomistic Modeling of a Graphene Copper Multilayered Conductor

Raju Ghimire[1,2], Pouria Khanbolouki[2], Ivana Gonzales[3], and Mehran Tehrani[2]

[1] Nanoscience and Microsystems Engineering, University of New Mexico, Albuquerque, NM, United States

[2] Department of Mechanical Engineering, The University of Texas at Austin, Austin, TX, United States

[3] UNM Center for Micro-Engineered Materials, Chemical & Biological Engineering Department, University of New Mexico, Albuquerque, NM, United States

Abstract: The addition of nanocarbons to copper (Cu), specifically in the form of graphene (GN), is reported to enhance copper's properties. GN-Cu nanocomposites can potentially achieve enhanced electrical, mechanical, thermal properties and lower temperature sensitivity of electrical resistivity compared with copper. These characteristics make GN-Cu materials interesting for several applications, including but not limited to interconnects, high current power lines, and elevated-temperature rotating machines. Charge conduction in these materials is controlled by microstructural features as well as nanoscale interfacial phenomena between the GN and Cu. However, systematic and random errors should be properly analyzed before reporting any dimension-dependent property improvement, specifically electrical conductivity. In this work, the electrical conductivity of GN-Cu multi-layered conductors is investigated using both experiments and atomistic simulations. Possible error sources that can result in inaccurate measurements of conductivity in thin metal films are discussed. While GN-Cu multi-layered conductors show slight conductivity improvements, their temperature coefficient of resistance (TCR) is reduced by 3.1 %. First-principles simulations show that the proximity of graphene and copper induces significant modifications in the electronic structure of graphene and copper, which can have crucial implications on the electron mobility in graphene and copper. For instance, our calculations show that in the GN-Cu hybrid the $3pz$-states of graphene can

strongly mix with the $3d$-states of copper and the Fermi energy of graphene is pushed to higher values resulting in the n-doping of graphene.

3.1 Introduction

Electrical conductors are the backbone of the energy industry. Conductors that outperform copper (Cu) are desired for electrical power, communications, electronics, and electric machines by many industries [10]. The electrical conductivity of most conducting metals follows Al<Au<Cu<Ag. Considering the cost and mechanical properties of silver, copper is the metal of choice for many applications. The need for more efficient electrical motors, transformers, and generators has driven extensive research efforts on improving copper's electrical conductivity. Metal matrix composites, adding nanomaterials to a metal, seem to be a promising candidate toward this goal [11, 47, 70]. For applications where lightweight is required, carbonaceous conductors have been developed and extensively researched. Two major groups of advanced conductors are currently under investigation, carbon-based and metal-based.

Carbon nanotubes (CNTs) and graphene are considered promising nanofillers for metals because of their exceptional physical properties [47, 71]. Until graphene discovery, CNTs were the dominant carbon nanofillers used in metal matrix composites (MMCs). Carbon nanotubes (CNT)-metal wires are emerging for lightweight conductors [72]. Their excellent thermal, mechanical, [73] and electrical [74-76] properties, including current-carrying capacity[77], hold great promise for the growing electrical power demands of future devices and vehicles. Adding a small amount of CNT improves copper's current carrying capacity and strength [46]. However, the poor affinity between CNT and metals hinders their promise of an ultra-conductor [46].

Along with CNTs, researchers are also working to take advantage of graphene's outstanding properties by incorporating them into metal matrices. Unlike CNT, graphene is easier to disperse into metals due to its better affinity for metals.

Graphene has similar intrinsic properties to CNTs and offers a larger surface area, potentially resulting in better transfer of its properties to the composite [47]. Thus, in the last decade, the metal matrix composites enhanced with graphene have drawn much attention to enhance metals' mechanical, electrical, and thermal properties [45, 70, 78-82]. Various processing techniques have been developed for copper graphene nanocomposites [3].

The performance of conductors is usually normalized to the International Annealed Copper Standard (IACS), which has an electrical conductivity of 58.1 MS/m at 20°C; copper's conductivity is therefore 100% IACS. Impurities, including alloying elements and oxides, and grain boundaries, degrade the electrical conductivity of copper. Single-crystal copper achieves a 109% IACS and 113% IACS upon hot isostatic pressing [63, 64]. Single-crystal silver's electrical conductivity was shown to improve with the addition of a small fraction of copper

[83]. This work shows that impurities, when properly incorporated, can improve the electrical properties of metals.

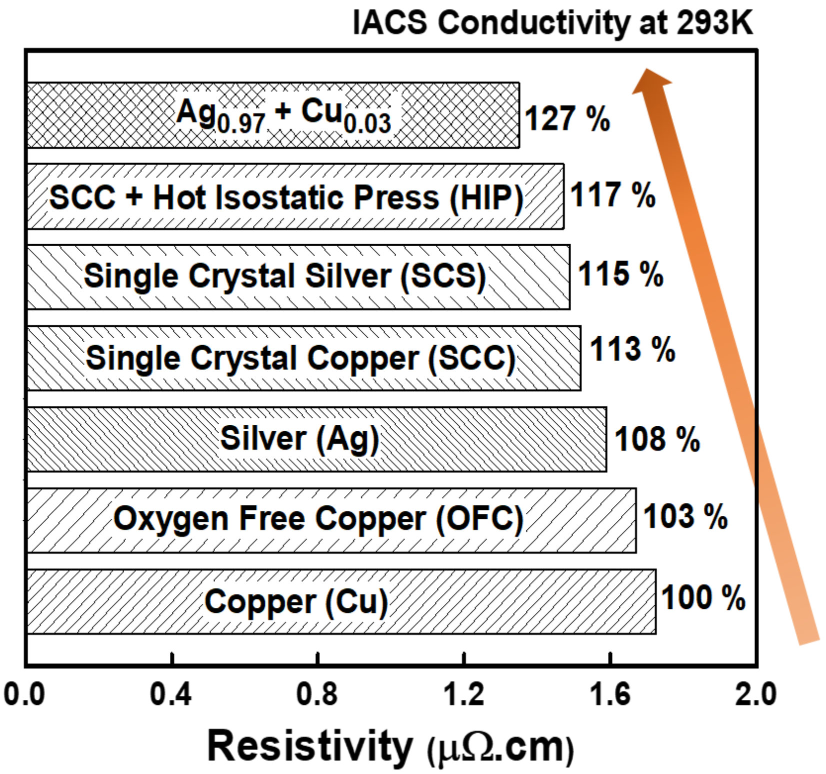

Figure 7: Electrical conductivity of polycrystalline conductors (Cu, OFC, and Ag) and single-crystal Cu (SCC), hot pressed SCC, single-crystal Ag, and single-crystal Ag0.97Cu0.03 alloy [19-21].

There are reports of enhanced physical properties for graphene-copper composites [32, 47]. Specifically, several studies have investigated improving electrical properties of copper by synthesizing high-quality graphene on copper foils using different fabrication approaches [2, 23, 24]. Most importantly, hot pressing several Cu foils with CVD-grown graphene on them (less than 50ppm) has resulted in multi-layered Cu-graphene films exhibiting an ultra-conductivity of 117% IACS; these results are yet to be reproduced by other groups [2]. The present study aims to reproduce the 117% IACS in multi-layered graphene-copper films. Studies reporting enhanced electrical conductivities often use small-scale samples that are not perfectly uniform in their diameter, thickness, etc. Measurement errors, therefore, need to be carefully weighed when reporting enhanced ultra-conductivities. In this work, multi-layered graphene-copper samples were fabricated and investigated from both a theoretical and experimental standpoint. Possible error sources for electrical conductivity measurements are investigated and discussed. Finally, the high-temperature conductivity of copper-graphene conductors is explained.

3.2 Experimental and Modelling

Experimental: Multi-layer chemical vapor deposition (CVD) grown graphene on ~50 μm copper foils were obtained from ACS materials. Graphene's quality and coverage were determined using Raman spectroscopy (Renishaw inVia) mapping with a He-Cd laser of wavelength 442 nm. The samples were then cut into circular disks and stacked, 3 to 10 foils, in a 20 mm diameter graphite mold. The stacked samples were then sintered for 10 min at 950 °C under a uniaxial pressure of 50 MPa in a medium vacuum (~mTorr) environment using Spark Plasma Sintering (SPS) technique.

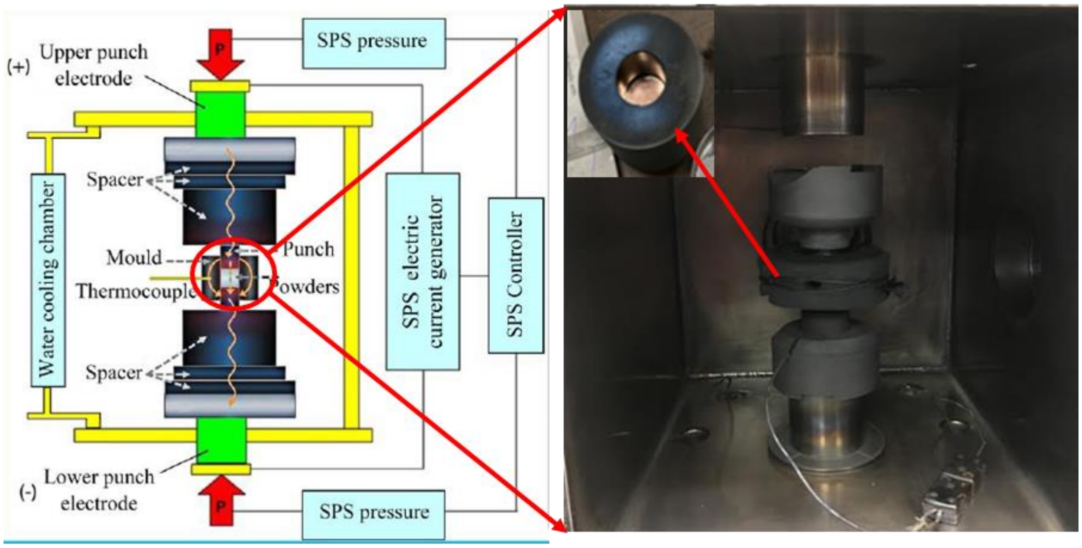

Figure 8: Schematic and actual Spark Plasma Sintering (SPS) setup.

SPS cross-sectional samples were then ground and polished using sandpaper up to a maximum grit of 1200 and $3\,\mu m$ diamond suspension. The sample thickness uniformity of about $\pm 5um$ was achieved, using PELCO 15000 micrometer lapping fixture, before characterization. A nano-voltmeter (2182) and DC-current source (6221) from Keithley were used to do the electrical measurement using the van der Pauw method. These measurements followed the ASTM standard B193. Electrical properties at elevated temperatures were characterized using a physical property measurement system (PPMS, DynaCool with thermal transport option). XRD (Rigaku Miniflex 600 Diffractometer) was used to study the crystalline structure. Crystal orientations were qualitatively investigated using XRD with $Cu\ K_{\alpha}$ radiation in the $\theta - 2\theta$ geometry. Additionally, sample thickness was measured using flat and pointed anvil Mitutoyo micrometers ($\pm 1\mu m$) as well as calculated from weight measurement. Image J software was used to calculate the sample area, and thickness was calculated using standard copper density from the equation:

$$t = m/(\rho_d \times A) \qquad (17)$$

Error analysis and uncertainty propagation can be estimated as follows:

The electrical resistivity (ρ) of a foil of thickness t can be written as [84]

$$\rho_f = \frac{\pi f(r)}{ln_2} t \frac{R_1+R_2}{2} \qquad (18)$$

where R₁ and R₂ are resistances and correlated, but 't' is measured independently. For uncertainty propagation analysis, the error, e, in resistivity measurement can be written as:

$$e_{\rho_f} = \sqrt{\left(\frac{\partial\rho}{\partial R_1}.e_{R_1}\right)^2 + \left(\frac{\partial\rho}{\partial R_2}.e_{R_2}\right)^2 + \left(\frac{\partial\rho}{\partial t}.e_t\right)^2 + 2\left(\frac{\partial\rho}{\partial R_1}\right)\left(\frac{\partial\rho}{\partial R_2}\right)e_{R_1}e_{R_2}} \qquad (19)$$

Replacing the following partial differentials in the e_{ρ_f} equation results in:

$$\frac{\partial\rho}{\partial R_1} = \frac{\partial\rho}{\partial R_2} = \frac{\pi t f(r)}{2ln_2} \text{ and } \frac{\partial\rho}{\partial t} = \frac{\pi f(r)}{lln_2}\frac{R_1+R_2}{2} \qquad (20)$$

$$e_{\rho_f} = \frac{\pi t f(r)}{2ln2}\sqrt{e_{R_1}^2 + e_{R_2}^2 + \left(\frac{R_1+R_2}{t}\right)^2 . e_t^2 + 2e_{R_1}e_{R_2}} \qquad (21)$$

The uncertainty in the measurements of the R₁, R₂, and t can be propagated to resistivity using the above formula.

Modeling: GN-Cu materials were studied using density functional theory (DFT) calculations with 5.12 Å × 5.12 Å × 41.82 Å unit cells containing 2-layers of graphene and 17-layers of Cu atoms with a total of 15 carbon atoms and 68 copper atoms. The stacking order of Cu layers on graphene, as shown in Figure 9, and the terminology was adopted from the literature [85].

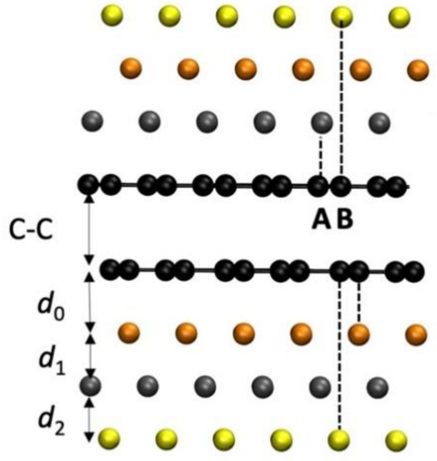

Figure 9: Stacking model of GN-Cu hybrid system used in the DFT calculations (only 2-layers of graphene and 6-layers of Cu atoms as shown). Black – C atoms; yellow, grey, and orange – Cu atoms in different layers.

All calculations were done using the density functional theory in pseudopotential plane wave implementation, with 8 × 8 × 1 gamma centered mesh, projector augmented wave (PAW) pseudopotentials, and tetrahedron method with Blöchl corrections as implemented in the Vienna Ab initio Simulation Package [86-89]. The plane wave basis cut was set to 520 eV. We have tested the performance of the Local-density approximation (LDA), as well as several Generalized Gradient Approximation (GGA) approaches (including the functionals with van der Waals correction) to find the optimal and most accurate approach for the description of the GN-Cu hybrid system.

3.3 Experimental Results and Discussions

Samples of graphene on copper foils were characterized using Raman spectroscopy. Figure 10 shows the Raman peaks and peak intensity ratios for each sample as well as 2D- to G-peak ratio mapping of a 2-layer (2L) graphene on copper. The sharpening of G-peak and broadening of 2D-peak occurs as the number of graphene layers increases. The peak intensity ratio shows that the number of graphene layers matches the supplier's claim. Raman mapping of the 2L graphene on copper over a 30×30 µm area shows that all the surface is covered with mostly 2L graphene.

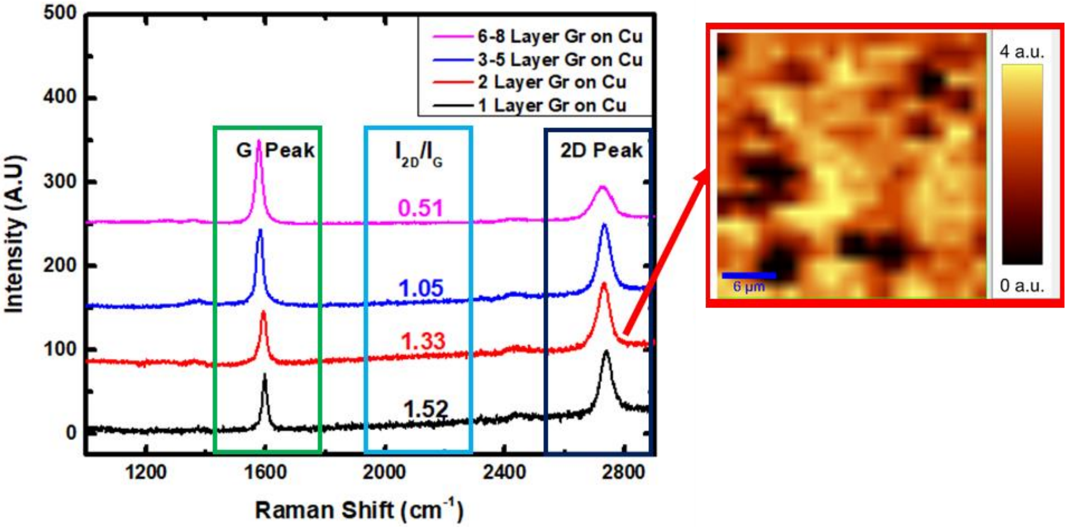

Figure 10: Raman spectra of CVD graphene on copper foils and 2D to G peak ratio mapping of 2-layer graphene on copper.

Copper-graphene samples fabricated in this study and elsewhere are usually tens of microns thick and sub-centimeter in lateral dimensions. Dealing with such small dimensions and variabilities introduced by sample preparations is somewhat difficult but critical as they can cause large uncertainties in conductivity measurements. Most importantly, film thickness measurements can introduce large errors to electrical conductivity.

To prevent thickness measurement errors, the effect of sample size and thickness as well as thickness measurement technique on the electrical conductivity of pristine copper foils was investigated. Sample thicknesses were measured using three different approaches, namely the density approach, a flat micrometer, and a pointed micrometer. The flat and pointed anvil and spindle (measuring faces) for the micrometers used in this study are shown in Figure *11*.

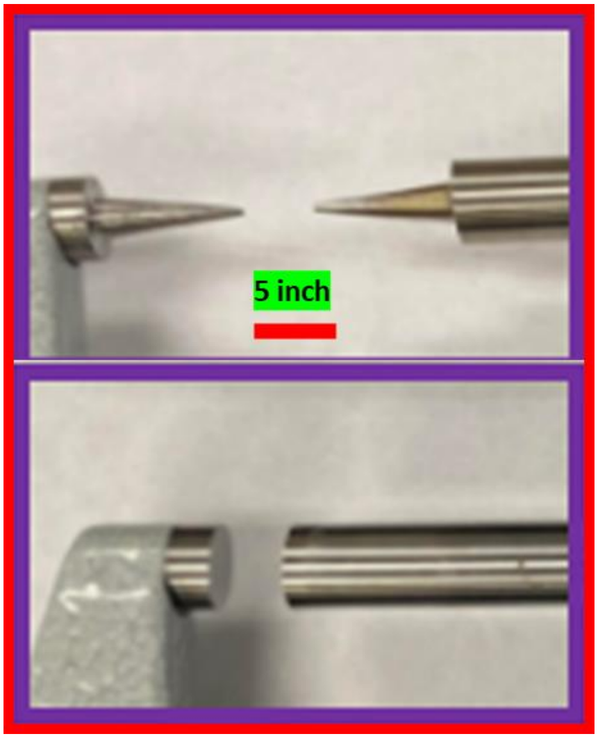

Figure 11: Pointed and flat anvil/spindle micrometers.

Three copper samples of 7, 50, and 125 μm nominal thicknesses were examined. Figure 12a shows the measured thickness values for each approach. The flat anvil micrometer measures a higher thickness than the nominal value, as the samples are not perfectly flat with respect to the anvil size. The pointed micrometer overcomes the issue of non-flat samples but might indent the samples, especially if they are not hard. Pointed micrometer measurements are, therefore, slightly lower than the nominal thicknesses. Thickness calculation from sample weight measurement (given that the density is known) comes with errors from sample area measurement. Thickness values measured using this approach seem to be more accurate in general with values that are in between the flat and pointed micrometer measurements. The corresponding errors in conductivity measurements for different thickness and size samples are plotted in Figure 12b. The flat micrometer is not suitable for any of the thickness ranges, whereas the density approach works best overall. Pointed micrometer works for copper samples that are 50 microns and thicker. Moreover, all the thickness measurement techniques are associated with different sources of error, which are inversely proportional to the sample thickness.

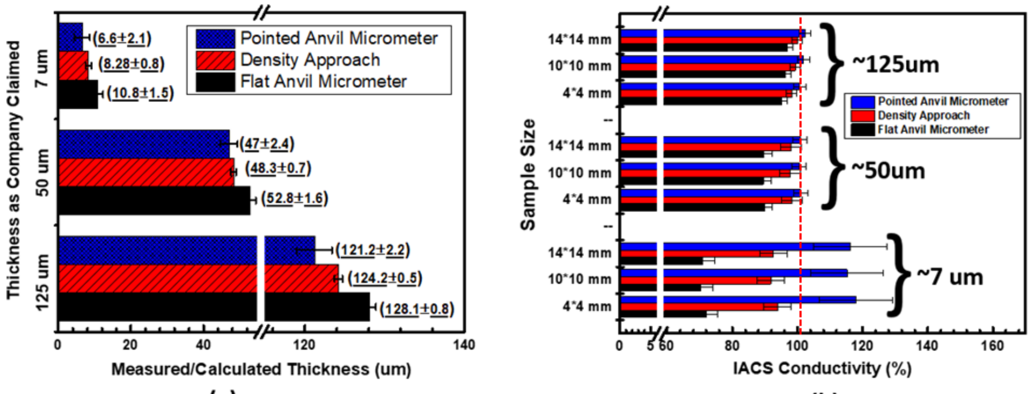

(a) (b)

Figure 12: Sample thickness and corresponding conductivity measurements using different thickness measurements techniques.

Next, the electrical conductivity of multilayered copper-graphene samples, consolidated via SPS, was measured. Pointed anvil measurements were employed due to their ease of use and to document thickness variations in samples; although the density approach gives similar or more accurate thickness measurements, it only provides an average value. Thicker samples were prepared by SPSing several foils with a total thickness of up to 200 µm. As shown in Figure 13a, an electrical conductivity of ~100% IACS was measured for multi-layered copper-graphene films that are thicker than 80 μm. Any improvements for thicker samples, with reference to copper's conductivity, are clearly within the measurement error deviations. Surprisingly, the 56 μm sample shows a conductivity of 114% IACS; this measurement is not correct, as explained later. A reference copper sample with a similar thickness to the 56 μm copper-graphene one was measured and exhibited a conductivity of 100% IACS.

To understand the 114% IACS anomaly, several samples with different lateral dimensions but an identical thickness of 47 μm were annealed at conditions similar to those experienced by the copper foils during the graphene growth and consolidation processes. A micrometer with a pointed (0.3 mm diameter) anvil and spindle was used. A ratchet stop was used to stop the anvil and spindle at a constant force when touching each sample. The thickness of the reference sample was measured as 47 μm, however, all annealed samples were measured as 43 μm. As shown in Figure 13b. While the reference copper sample demonstrated the right conductivity value, all annealed samples showed an enhanced conductivity regardless of their size. The higher conductivity is due to the lower measured thickness of the annealed samples, as confirmed by microscopic images shown in Figure 14b. It can be concluded that the thickness measurement approach is not suitable.

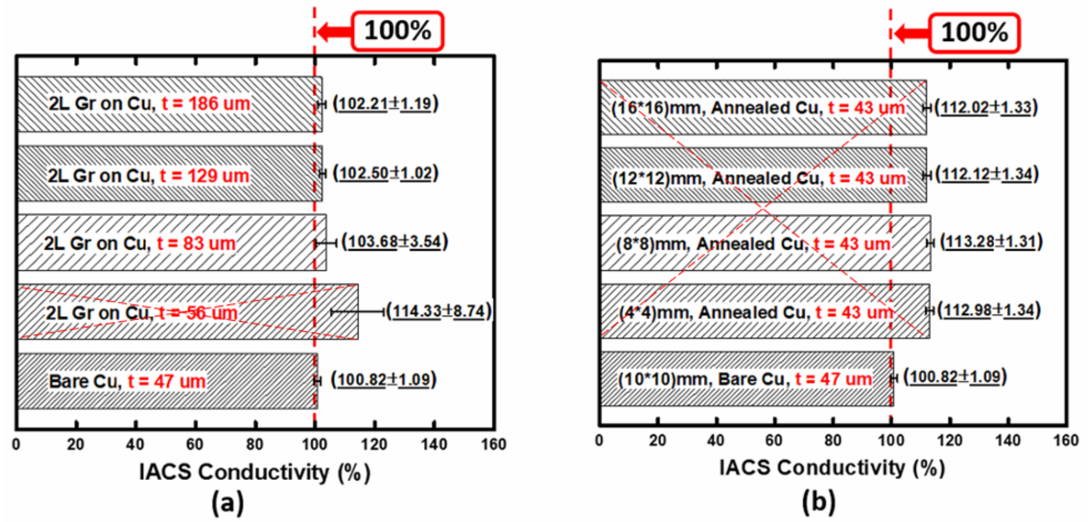

Figure 13: Electrical conductivity of (a) different thickness SPS samples and (b) different size annealed copper compared to bare copper. Crossed measurements are not correct.

To understand the discrepancies in thickness and conductivity measurements, the sample surface was investigated under an optical microscope. Figure 14 shows the sample surface of reference and annealed copper. The pure copper surfaces remain the same after the thickness measurement, whereas the micrometer leaves indents (marked with circles on the figure) on the annealed copper due to its low hardness. For the studied films of 47 µm thickness, the measurement is off by 4 µm (2 µm on each side), resulting in a 9% higher electrical conductivity. It also seems that the high-temperature annealing increases grain sizes (inset in Figure 14b), thus improving the conductivity by a few percentages. Overall, the conductivity of annealed samples is ~11-12% higher than the reference copper sample. For thicker samples of the same hardness, the same thickness measurement error (~4 µm) only results in a small inaccuracy of the measured conductivity.

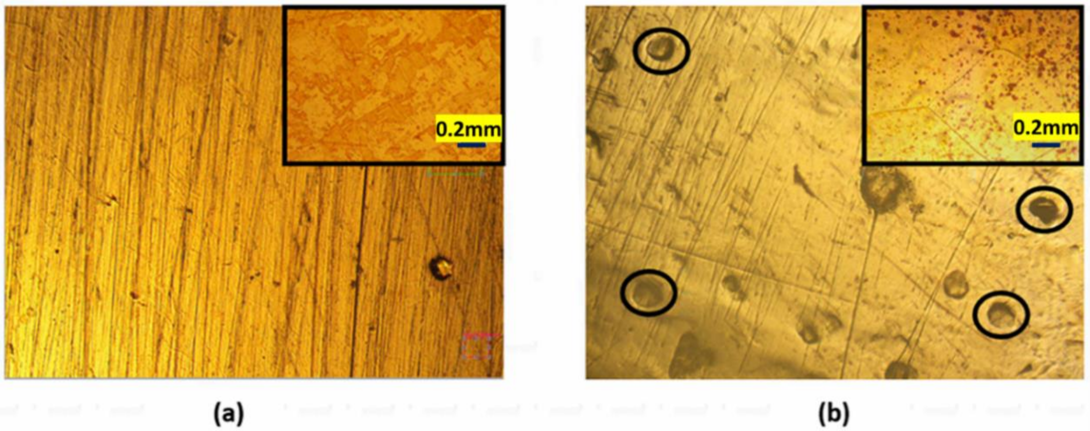

Figure 14: Sample surface after the thickness measurement using micrometer (a) Bare Cu and (b) Annealed Cu. Scale bars are for insets.

Proper analysis of the experimental data is of utmost importance in every aspect of research, in particular in advanced conductor research, where most of the samples are in the shape of thin films or irregular cross-section wires. In particular, uncertainty propagation should be taken into account in the statistical analysis of the experimental data [90].

Several SPS copper-graphene samples were characterized using the pointed micrometer. These samples consistently showed misleadingly high conductivities between 107 to 114%IACS due to thickness measurement error discussed earlier. These samples were between 56-65 μm as measured with the pointed micrometer. However, similar but thicker samples only achieved 101-104%IACS.

The temperature-dependent resistivity of samples was carried out from 20 to 400 K at intervals of 1 K using the van der Pauw method. The results in Figure *15* show that the variation of electrical resistance normalized by room temperature resistance for reference copper (black), copper with a 2-layer (2L) graphene grown on it (red), and multi-layered sample made by consolidating 2L graphene-copper (blue). To understand different conduction mechanisms, the dominant electron scattering factors over different temperature ranges should be considered, as summarized in Figure 16.

Below 70 K, where impurities are the dominant contributor to electrical resistance, pure copper exhibits a slightly lower resistance than other samples. The reference copper foil and the ones with graphene were from different sources and therefore of dissimilar qualities. On the other hand, all of the samples show a similar trend from 70 to 300 K, where grain boundaries are the dominant scattering mechanisms contributing to resistance, suggesting that the contribution of grain boundaries on the electrical resistance is not significant in these samples. From 300-400 K, where phonon scattering is the major component contributing to electrical resistance, the graphene-copper samples have a lower normalized resistance than copper. As explained below, the texture (preferred crystalline orientation) developed during SPS in copper helps reduce phonon scattering, which in turn improves the electrical conductivity at 390 K by more than 3%.

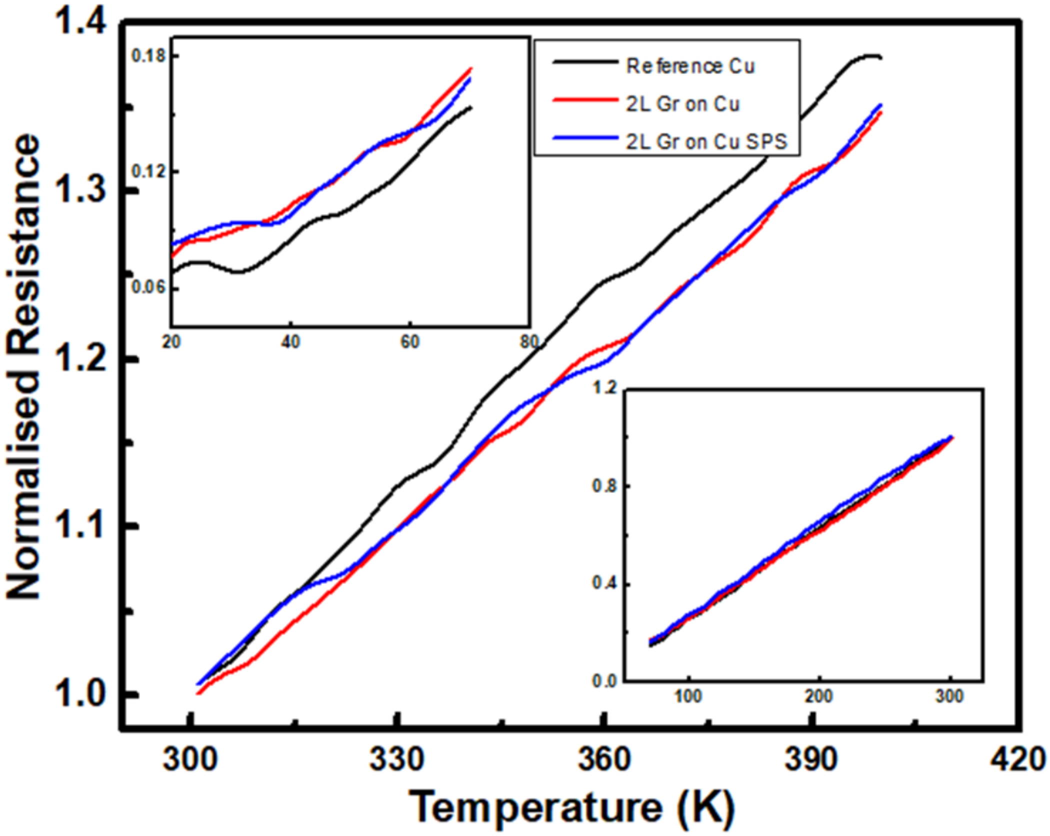

Figure 15: Normalized resistance versus temperature of different samples from 20 to 400K.

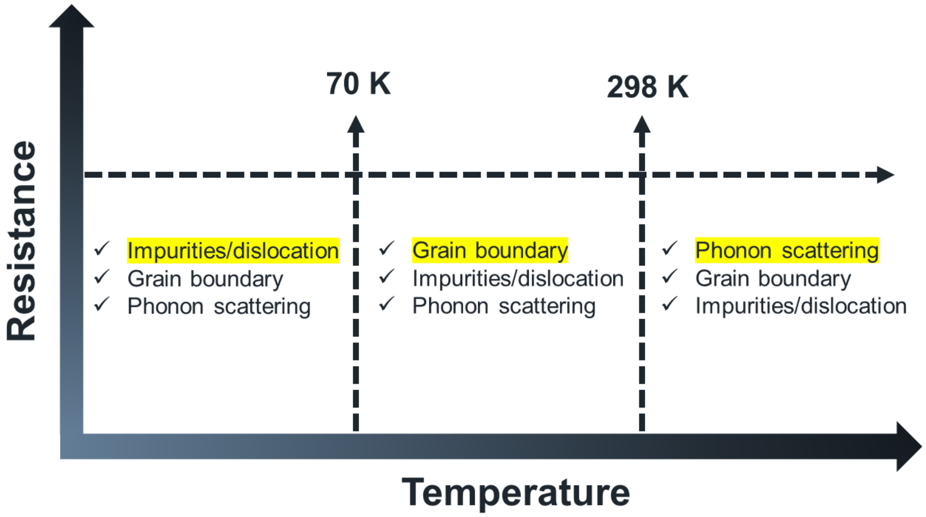

Figure 16: Dominant resistance mechanisms at a different temperature range [19, 21, 25-30].

Figure 17a shows that the crystal orientation of graphene grown copper with respect to the polycrystalline copper sample. During graphene growth, the texture developed on copper, and it changes along with the number of graphene layers. The texture development in copper, either due to the sintering parameter or gas environment or graphene growth, is still unclear, and great discussion is going on through the scientific community[91-96]. Graphene has a hexagonal crystal structure. Copper (111) crystals are also hexagonal, and it seems that the graphene templating effect induces a (111) texture in copper. Additionally, as the pressure or time increases for the higher number of graphene layers, the copper texture shifts to the high-index facets.

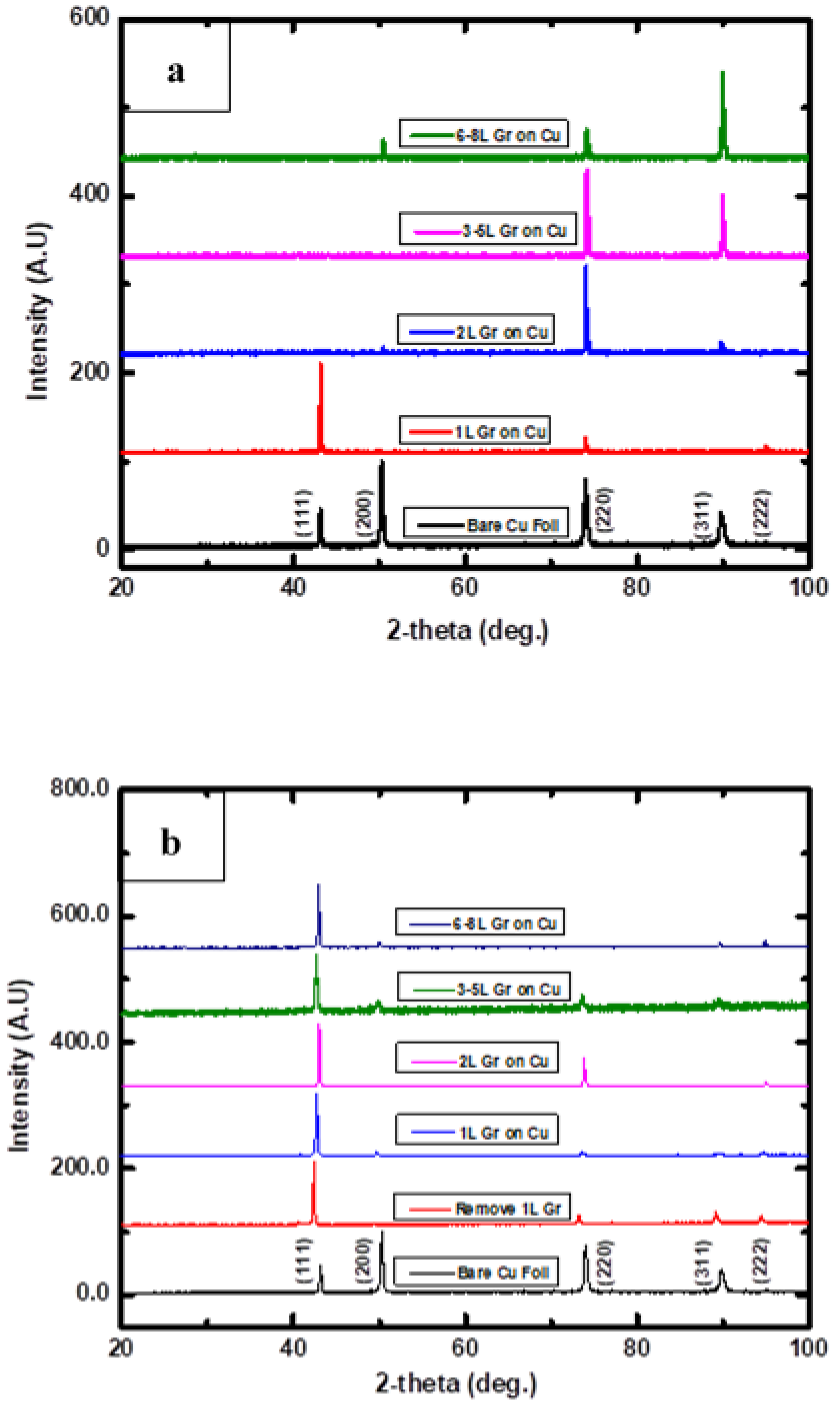

Figure 17: (a) XRD of polycrystalline and different layer graphene grown copper foil, (b) XRD of polycrystalline and SPS of different layer graphene grown copper.

However, Figure 17b demonstrates that the copper crystal reorients mostly in the (111) direction under uniaxial pressure at high temperature in a vacuum (mtorr) environment. In fcc crystals, (111) slip plane is favorable with <110> slip direction, which is why copper texture developed in (111) direction during sintering at high-temperature and uniaxial pressure [85]. Additionally, the XRD pattern of SPS samples, even after removing the graphene layer, also shows that the texture development in (111) direction. In summary, copper texture shifts to higher index facets as the sintering time and gas pressure increases but under uniaxial mechanical pressure, it will only orient in (111) directions. As discussed earlier, the few percent improvements in electrical conductivity might arise from the texture developed in (111) direction, as shown in Figure 17b during the SPS process.

3.4 Structure optimization of the GN-Cu hybrid system using different DFT functionals:

In this study, the interface structure and the binding energy between the copper(111) and graphene were studied as described by LDA, GGA-PBE approach, and DFT-D2 method of Grimme, where the van der Waals interactions are described via a simple pair-wise force field. All the structures considered in our study were allowed to relax fully. Following the terminology [85], we defined the interface configuration as top-hcp when A and B graphene layers overlap with the first and second layers of Cu. In top-fcc configuration (shown in Figure 9) A and B layers of graphene overlap with the first and third layer of Cu, while in hcp-fcc configuration A and B layers of graphene overlap with the second and third layer of Cu. The binding energy between graphene and copper was defined as $\Delta E_{\text{GN-Cu}} = E_{\text{GN-Cu}} - (E_{\text{GN}} + E_{\text{Cu}})$ where $E_{\text{GN-Cu}}$, E_{C}, and E_{Cu} are energies of the hybrid GN-Cu system (isolated graphene bilayer and metal substrate), respectively. Table 4 shows that the PBE-GGA approach results in the non-favorable binding of copper and 2-layer graphene as cohesion energy between Cu and graphene is positive. LDA and GGA approach based on DFT-D2 predict favorable interaction energy between copper and graphene in all the hybrid interface configurations. Cohesive energies calculated using the LDA approach are much smaller than the ones calculated using vdW-corrected functional, ranging between −5 and −7 meV per atom. DFT-D2 method is the only method that predicts top-fcc configuration as the most stable GN-Cu hybrid structure with the interaction energy of −21 meV per atom. This configuration was found to be the most stable of GN-Cu hybrids in previous work by Xu and Buehler [97].

Table 4: Energy (in eV) and binding energy ($\Delta E_{\text{GN-Cu}}$) per atom of different Cu-C structures calculated with different DFT approaches.

	top-fcc	top-hcp	hcp-fcc
GGA-PBE	-4.714 $\Delta E_{\text{GN-Cu}}$=+0.003	-4.766 $\Delta E_{\text{GN-Cu}}$=+0.001	-4.670 $\Delta E_{\text{GN-Cu}}$=+0.002
LDA	-5.671 $\Delta E_{\text{GN-Cu}}$=-0.007	-5.714 ($\Delta E_{\text{GN-Cu}}$=-0.004)	-5.628 $\Delta E_{\text{GN-Cu}}$=-0.005
DFT-D2	-5.076 $\Delta E_{\text{GN-Cu}}$=-0.021	-5.122 $\Delta E_{\text{GN-Cu}}$=-0.020	-5.033 $\Delta E_{\text{GN-Cu}}$=-0.017

The geometric parameters of the GN-Cu hybrid were further analyzed. A comparison between the data calculated for the hybrid GN-Cu system (

Table 5) and the ones calculated for both bulk copper (Table 6) and the 2 –layer graphene (Table 7) shows that GGA-PBE reproduces metal structural parameters well but underestimates the binding between graphene layers in graphene. Namely, the C-C interlayer distance in graphene is calculated as 3.85 Å, which is overestimated for 0.5 Å as compared to the experimental interlayer distance in graphene. The LDA approach reproduces experimental C-C interlayer distance in graphene but gives the largest error in structural parameters of the metal. The LDA approach calculates 3.35 Å for the C-C interlayer distance in graphene, which is in excellent agreement with the experimental value, but for the cell parameter of the bulk copper yields 5.00 Å, which is underestimated by 0.15 Å compared to the experimental Cu cell parameter. The DFT-D2 approach describes reasonably well structural parameters of both the metal and graphene. The DFT-D2 calculated C-C interlayer distance in graphene is 3.33 Å, while the cell parameter of copper is predicted as 5.07 Å, which is only 0.09 Å smaller than the experimental value.

For the top-fcc GN-Cu hybrid structure, the GGA-PBE predicts the largest C-Cu distance of 3.56 Å. Based on the PBE-GGA description of the cohesive energy and C-Cu binding distance in the hybrid, we can conclude that this approach fails in capturing favorable copper-graphene interaction in the GN-Cu material. LDA gives the smallest C-Cu distance in the hybrid of 2.48 Å. This value is still 0.24 Å larger than predicted in previous work [85, 97] for the graphene/Ni(111) model. The discrepancy could be explained by the difference in the GN-Cu models used in this and previous work. Namely, Xu and Buehler use a smaller model with one graphene layer and only four layers of Cu. The difference might also be because the cell parameters of the hybrid are fully relaxed, while in the previous work cell parameters of the hybrid were set to that of a bulk metal. DFT-D2 method predicts a C-Cu distance of 2.86 Å, which is intermediate to that of the GGA-PBE and the LDA calculated values.

Table 5: Geometrical parameters of top-fcc GN-Cu structure calculated with different DFT approaches.

	GGA-PBE	LDA	DFT-D2	DFT-D3
a/Å	5.05	4.97	5.00	5.00
C-Cu layer/Å	3.56	2.48	2.86	2.99
C-C layer/Å	3.39	3.25	3.08	3.33
$\Delta E_{\text{GN-Cu}}$/eV at^{-1}	+0.003	-0.007	-0.021	

Table 6: Geometrical parameters of bulk copper calculated with different DFT approaches.

	GGA-PBE	LDA	DFT-D2	DFT-D3	exp
a/Å	5.16	5.00	5.07	5.06	5.122
Cu-Cu layer/Å	2.08	2.02	2.05	2.05	2.091

Table 7: Geometrical parameters of 2-layer graphene calculated with different DFT approaches.

	GGA-PBE	LDA	DFT-D2	DFT-D3	exp
a/Å	4.94	4.89	4.93	4.94	4.928
C-C layer /Å	3.85	3.35	3.33	3.36	3.335

None of the DFT approaches used here resulted in the C-Cu binding distance smaller than 2.48 Å. Therefore, we used the LDA and the DFT-D2 to construct a Cu-C hybrid model in which the cell parameters of the hybrid were fixed to the cell parameters of bulk copper. In this model (Table 8 and Figure 9), the LDA approach results in a C-Cu binding distance of 2.21 Å, matching well the literature [97] results. The vdW-corrected DFT-D2 functional results in a larger binding distance between copper and graphene of 2.78 Å. Our results thus confirm findings from previous work that the LDA approach provides a reasonably accurate description of the graphene-metal interface. Therefore, the results presented further are obtained using the LDA approach. The convergence of the results with respect to the size of the GN-Cu hybrid model (number of Cu layers) and Cu-C binding distance was still tested.

Table 8: Optimized geometry of GN-Cu hybrid where *a* and *b* lattice parameters set to that of experimentally determined bulk Cu cell parameters. $E=E_{GN\text{-}Cu}-(E_{GN}+E_{Cu})/2A$, where A is the surface area.

	LDA	DFT-D2
C-C layer/Å	3.13	3.16
C-Cu; d_0/Å	2.21	2.78
Cu-Cu; d_1/Å	1.96	2.01
Cu-Cu; d_2/Å	2.00	2.02
*E/eVÅ^{-2}	**-32.1**	-41.2

(a) Electronic structure and charge transfer on the GN-Cu interface:

Figure 18 shows the projected density of states and band structure of 2-layer graphene and bulk copper obtained using the LDA approach. The results are in good agreement with the previously reported density of states and band structure of pure copper and 2-layer graphene, which confirms the reliability of the LDA approach. For example, the LDA approach correctly predicts 2-layer graphene as a zero-band gap semiconductor in which the edges of the valence and conduction band are composed of $2p_z$ states of carbon.

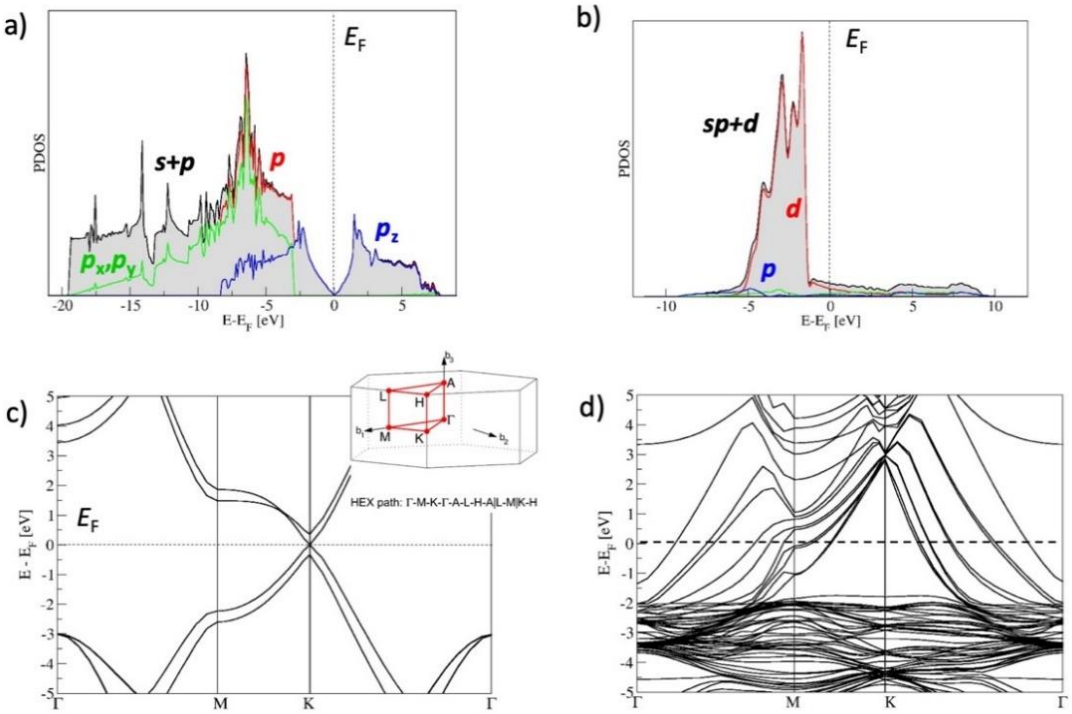

Figure 18: a) Projected density of p states in 2-layer graphene; b) Projected density of states of Cu; c) Band structure of 2 -layer graphene along Γ-M-K-Γ path; d) Band structure of Cu along Γ-M-K-Γ path as calculated with LDA approach.

We further performed the charge analysis using Bader's theory. Figure *19* shows the difference in charge $\Delta\rho=\rho(\text{GN-C})-\rho(\text{Cu})-\rho(\text{GN})$ along the vertical axis perpendicular to the graphene surface, where $\rho(\text{GN-C})$, $\rho(\text{Cu})$, and $\rho(\text{GN})$ are charges calculated for the hybrid GN-Cu system, isolated graphene bilayer, and metal substrate, respectively. The results show that charge accumulation and depletion areas form a charge distribution dipole between the Cu-graphene surface. Furthermore, this analysis shows that the electrons are transferred from copper to graphene resulting in *n*-doping of graphene. The charge transfer from copper to graphene is calculated as 0.78*e* per unit cell with an area 22.702 $Å^2$ (1 to 16 C atom ratio) in the model in which the hybrid cell parameters are set to bulk Cu and 0.502 per unit cell with area 22.08 $Å^2$ for the model in which the cell of the GN-Cu hybrid is allowed to relax fully. This result agrees with the finding that *n*-

type doping of graphene occurs when the work function of the metal is <5.2 eV[27, 98].

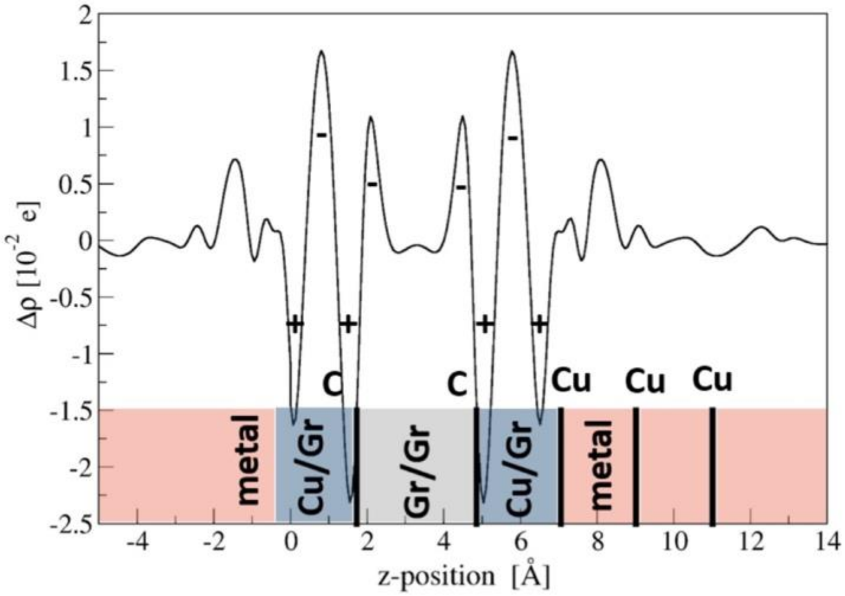

Figure 19: Charge difference $\Delta\rho=\rho$(GN-Cu)-ρ(Cu)-ρ(GN) along the vertical axis. $\Delta\rho>0$ stands for charge accumulation (-) and $\Delta\rho<0$ stands for charge depletion (+), which forms the charge distribution dipole between the GN-Cu surface.

Figure 20 shows the density of electronic states and band structure of the GN-Cu model calculated using the LDA approach. Comparing the projected density of states in GN-Cu hybrid compared to the density of states of graphene (Figure 20a and Figure 20c) shows that the Fermi level (E_F) of graphene in the GN-Cu hybrid is pushed to higher values as compared to pure graphene resulting in the non-zero density of states at Dirac point. This result is consistent with the electron density being transferred from copper to graphene resulting in *n*-doping of graphene. The band structure of GN-Cu hybrid with the marked contribution of C-atom 2p$_z$ states to each Kohn-Sham state (Figure 20c) shows that C-2p$_z$ states are strongly mixed with the Cu 3d-states, allowing for electron transfer between copper and graphene.

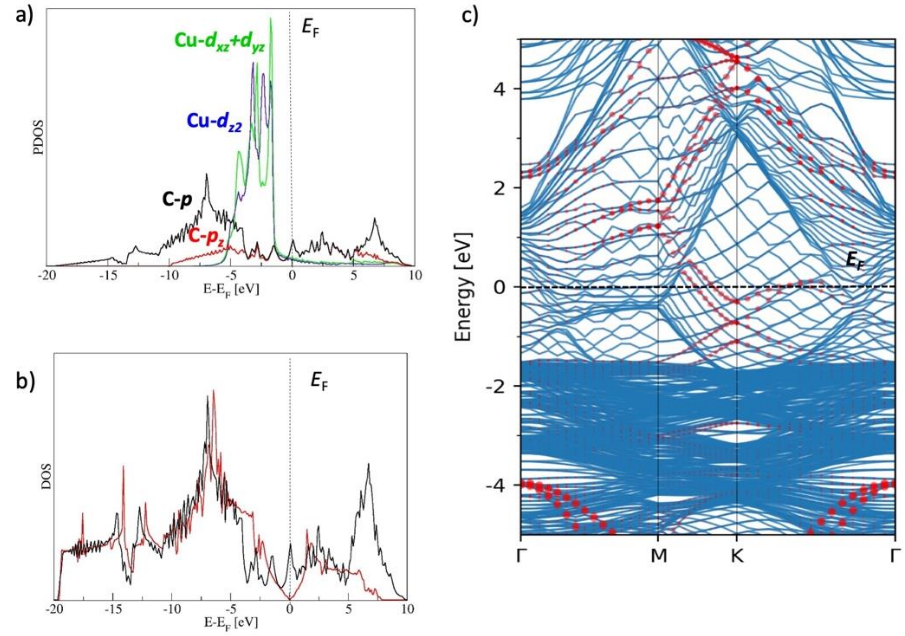

Figure 20: a) Projected density of states in GN-Cu hybrid; b) Comparison in the density of states of graphene in GN-Cu hybrid (black) and 2-layer graphene (red); c) Band structure of GN-Cu hybrid with the contribution of C $2p_z$ states to each KS state of a hybrid marked with red dots. Results are calculated using the LDA approach.

3.5 Conclusions

Thickness measurement errors, measured via standard micrometers, introduce large variations in electrical conductivity of thin foil samples (<50um), and as the samples become thicker (>100um), the effect of measurement errors becomes smaller. This work demonstrated the importance of proper error analysis and choice of measurement technique for thin conductor foils. Our results show that all measurement values should be reported with their associated error values calculated from uncertainty propagation analysis. The performance of GN-Cu samples from 300-400K is improved by 3.1% over pure copper due to the developed texture in the samples. However, graphene didn’t enhance conductivity in the studied samples. DFT results show that in the GN-Cu composite the $3pz$-states of graphene are strongly mixed with $3d$-states of copper, providing a non-zero density of electronic states at Dirac point. Additionally, the Fermi energy of graphene is pushed to higher values resulting in *n*-doping of graphene. Results also showed that the majority of electrons can get trapped at the interfaces and could move along the interfaces, potentially with ultrahigh mobilities.

Chapter 4. Electrical Properties of Graphene Coated Copper Wires Subjected to Hot Isostatic Pressing (HIP)

Raju Ghimire[1,2], Pouria Khanbolouki[2], and Mehran Tehrani[2]

[1] Nanoscience and Microsystems Engineering, University of New Mexico, Albuquerque, NM, United States

[2] Department of Mechanical Engineering, The University of Texas at Austin, Austin, TX, United States

Abstract: Hot isostatic pressing (HIP) offers an extra processing knob, i.e., pressure, besides time and temperature, to steer the microstructure of metals. HIP can drive recrystallization, limit grain growth, and in some cases, enhance grain growth. HIP is often utilized to eliminate internal porosity or enhance interfacial bonding in composites and nanocomposites. HIP has been shown to enhance the electrical conductivity of single-crystal copper. Similarly, hot uni-axial pressing of copper-graphene multi-layered films has shown to alter their microstructure and conductivity. This chapter aims to understand the underlying mechanisms responsible for changes in electrical properties of metal-graphene composites. In particular, the effect of HIP on several graphene-copper samples prepared under various conditions is investigated. The results do not show that HIP or graphene coatings improve copper's electrical conductivity or current carrying capacity.

4.1 Introduction

Nanocarbon-based conductors and metal-nanocarbon conductors are the two broad categories of room temperature advanced conductors. Advanced conductors can offer advantages over pure metals, such as improved mechanical properties, lighter weight, and higher current carrying capacity [99-102]. One metal-nanocarbon conductor that has been the focus of research in the past few years is the copper containing small loadings of graphene (GN). A 103-105% international annealed copper standard (IACS) for GN-Cu conductors with less than 0.001% graphene loadings has been reported in the literature [9, 103]. There is also a report of a GN-Cu conductor with 117% IACS [8], but this result has not been independently reproduced; see chapter 3.

The interaction between graphene and metals occurs via chemisorption or physisorption. Chemisorption requires bond formation while physisorption involves interactions between graphene's vacant p_z-orbital and (transition) metal's d-orbital [104]. However, copper doesn't have an affinity for carbon, and it is extremely difficult to properly design a GN-Cu interface that will allow for electron delocalization [105]. A properly designed interface between copper and graphene will allow the abundant electrons in copper to flow through high mobility graphene paths, resulting in higher conductivity for the composite. Graphene damage due to harsh fabrication conditions, graphene wrinkles, and graphene agglomeration are other challenges in obtaining an ideal GN-Cu interfacial bond.

Different processing techniques have emerged for the fabrication of GN-Cu composites with improved properties. Most of these techniques focus on achieving a homogeneous dispersion of graphene in the copper matrix. Some have also focused on developing a strong interfacial bond between the two components. These methods include powder metallurgy [106-108], spark plasma sintering [109, 110], electrochemistry [111, 112], cold spraying [113], roll bonding [114, 115], chemical vapor deposition (CVD) [45, 116, 117], in-situ growth [118], and metal infiltration [119] to obtain the target interfacial adhesion and overall improved properties for the composite.

Consolidation methods such as spark plasma sintering and hot isostatic pressing (HIP) are among the most useful processing tools in this field of research. In the HIP, the material is sintered under isostatic pressure and elevated temperatures. Various mechanisms such as plastic deformation, creep, diffusion, and densification can contribute to the changes in microstructure and properties of a material. One report [63] has shown that HIP decreased the electrical resistivity of single crystal copper by 5.5%. Another report has shown that uni-axial hot pressing of copper films coated with CVD graphene results in drastic microstructural and property changes [8]. However, the effect of HIP on the electrical properties of GN-Cu wires has not yet been investigated, to the best of the authors' knowledge. In this work, atomically thin graphene layers are grown on copper wires via CVD, and the resulting samples are hot-pressed iso-statically. The effect of HIP on the electrical properties of the GN-Cu wires is investigated and correlated to the structure and surface morphology of the wires.

4.2 Experimental Methods

Copper wires (99.99% pure from Sigma Aldrich) were cut to the desired dimensions and treated in a 0.1M ammonium persulfate (APS) solution for 30 min to remove the native copper oxide layer as well as any other surface contaminations. This treatment was followed by cleaning with acetone, isopropyl alcohol (IPA), and de-ionized (DI) water bath, respectively. The treated samples were placed in a quartz tube positioned in the middle of the CVD furnace.

Six samples, each comprising of 20 cm long wires, were prepared and treated according to the design of experiments described in Table 9. The reference samples were 30 AWG oxygen-free copper wires. The annealed samples were treated at 1030 °C under 10 SCCM of hydrogen flow for 30 minutes. Two layers of graphene were grown on the last set of samples. One sample from each set was treated with oxygen plasma etching, and finally, all the samples were HIPed as described later.

Table 9: Design of Experiments

	Reference Sample		Annealed Sample		Graphene Grown Sample	
Plasma Etch	Yes	No	Yes	No	Yes	No

The number of graphene layers, two layers in this case, was controlled following the previous work performed on the LPCVD system at UT-Austin [120]. The following steps were carried out to grow two layers of graphene on 30 AWG copper wire : (a) the quartz tube was pumped down to 10 mTorr, (b) the copper wire was heated to 1030 °C at a heating rate of 10 °C/min under a 10 standard cubic centimeters per minute (SCCM) flow of hydrogen gas, (c) the CVD pressure was set to 10 mtorr by adjusting the downflow valve, (d) graphene growth was conducted with introducing a mixture of hydrogen (10 SCCM) and methane (0.1 SCCM) for 30 min at 1030 °C, (e) the entire CVD system was naturally cooled under the same gas mixture flow. Annealed samples were treated under identical conditions but without introducing a carbon source, i.e., methane. The Graphene's quality was determined using Raman spectroscopy (Renishaw inVia) with a He-Cd laser of wavelength 442 nm. Raman spectroscopy was conducted on the samples right after the graphene growth and after the oxygen plasma was used to remove the graphene.

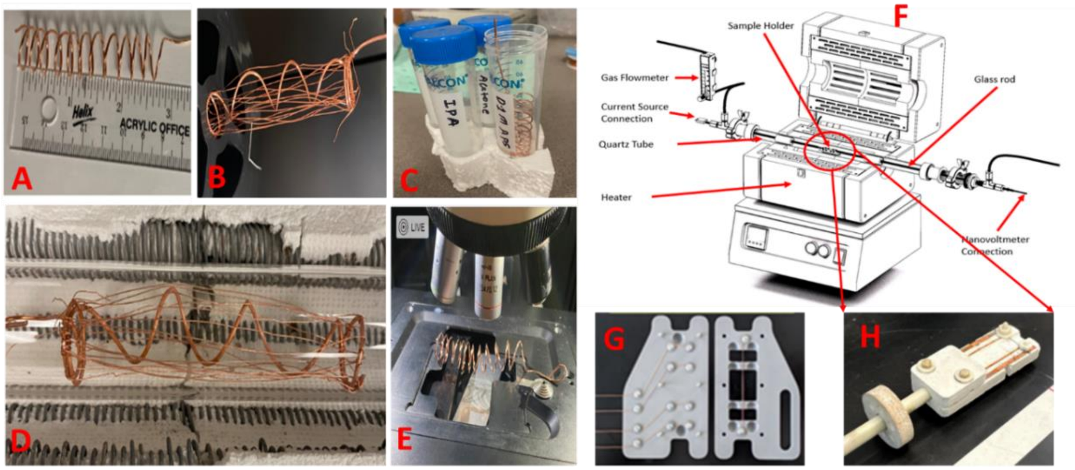

Figure 21: Graphene grow process and characterization setups: (A) 18AWG spiral wire sample holder, (B) 30 AWG wire winding on 18 AWG spiral wire, (C) Wire cleaning before graphene growth, (D) Sample inside furnace glass tube before graphene grow, (E) Raman spectroscopy measurement setup, (F and H) Elevated temperature resistance measurement setup, (G) Room temperature resistance measurement setup.

A Samco RIE-1C reactive ion etcher was used to remove graphene from copper wires using oxygen plasma. To investigate the effect of plasma etching on copper wires, besides graphene removal, one sample from each set was treated under the same condition. The samples were etched for 20 sec while oxygen flow rate and chamber pressure were maintained at 10 SCCM and 110 mTorr, respectively. The radiofrequency (RF) power was set to 70 W. The etching setup and samples are shown in Figure 22.

Figure 22: Reactive ion etching setup and samples: (A) Gas supply, (B) Etching chamber, (C) RF generator, (D) Sample preparation.

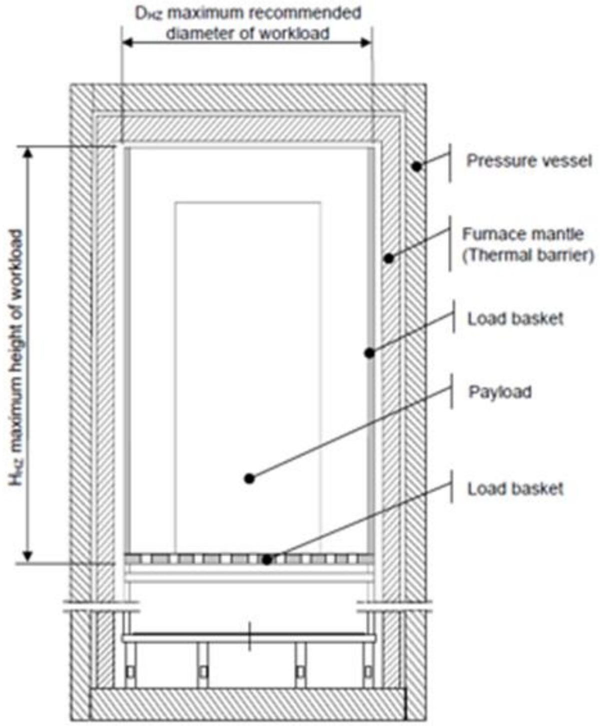

Figure 23: Hot isostatic pressing schematic.

The hot isostatic pressing (HIP, model Q1H15L Moly URC, Quintus Technology), schematically shown in Figure 23, was used to simultaneously apply the temperature and iso-static gas pressure. All samples were placed in the HIP chamber for 120 min at an Argon gas pressure and temperature of 100 MPa and 950 °C, respectively. The electrical conductivity of each sample was measured before and after the HIP treatment. A four-point probe setup connected with a nano-voltmeter (2182) and DC-current source (6221), both from Keithley, was used to measure the electrical conductivity of samples at room and elevated temperatures. The four-point probe electrical conductivity measurement followed the B193 ASTM standard. The wire diameter was measured using a Ratchet stop Mitutoyo digital micrometer with an accuracy +/- 1.27 micron. Wire diameters were also calculated by measuring their weight, length, and standard copper density; diameter = [(4 x mass) / (π x length x density)] ^0.5.

Ampacity measurements were carried out on 10 cm long wires. An Eventek current source (0-32V, 0-10.2A) with an accuracy of 0.01V and 0.001A was used to apply a constant current (cc) until the sample broke and the corresponding time was recorded. For comparison, 10 Amps of current was applied to each sample, and the fusing time was recorded under both vacuum (10^{-6} torr) and air environments.

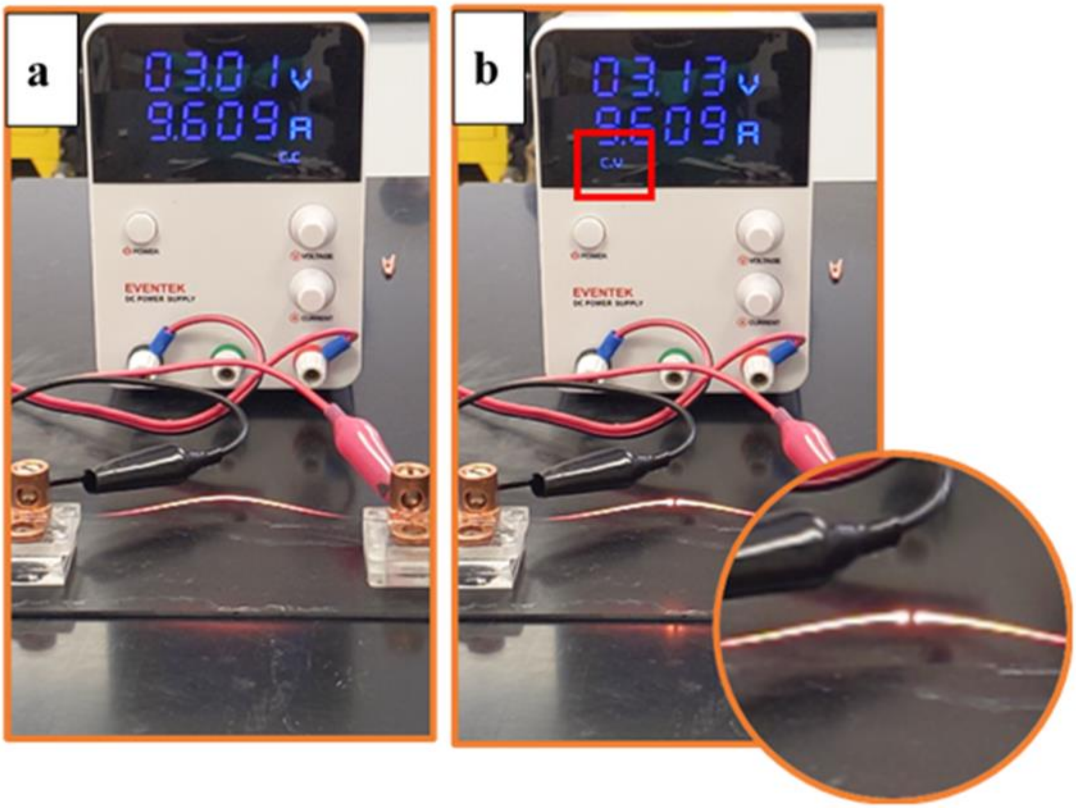

Figure 24: Demonstration of ampacity measurement before (a) and after (b) the wire fuses using 9.609A current.

Samples crystalline structures were probed using XRD, Rigaku Miniflex 600 Diffractometer. Grain orientations before and after the HIP treatment were qualitatively investigated using XRD with $Cu\ K_{\alpha}$ radiation in the $\theta - 2\theta$ geometry.

Conductivity measurement uncertainties for wire samples can be estimated using the following calculations. The electrical resistivity (ρ) of a wire of length L, resistance R, and cross-sectional area A can be written as:

$$\rho_w = \frac{RA}{L} \tag{22}$$

where R and L are measured independently, and $A = \pi D^2/4$. For uncertainty propagation analysis, the error, e, in resistivity measurement can be written as:

$$e_{\rho_w} = \sqrt{\left(\frac{\partial\rho}{\partial R}.e_R\right)^2 + \left(\frac{\partial\rho}{\partial A}.e_A\right)^2 + \left(\frac{\partial\rho}{\partial L}.e_L\right)^2} \tag{23}$$

Similarly, error for the cross-sectional area measurement is:

$$e_A = \left|\frac{dA}{dD}\right| e_D \tag{24}$$

Replacing the following partial differentials in the e_{ρ_w} equation results in (25):

$$A = \frac{\pi}{4}D^2 \rightarrow e_A = \frac{\pi}{2}De_D$$

$$\frac{\partial\rho}{\partial R} = \frac{A}{L} \; \& \; \frac{\partial\rho}{\partial A} = \frac{R}{L} \; \& \; \frac{\partial\rho}{\partial L} = -\frac{RA}{L^2}$$

$$e_{\rho_w} = \sqrt{\left(\frac{A}{L}.e_R\right)^2 + \left(\frac{R}{L}.e_A\right)^2 + \left(-\frac{RA}{L^2}.e_L\right)^2} \tag{25}$$

The uncertainty in the R, D, and L measurements can be propagated to the resistivity using the above formula.

4.3 Results and Discussion

Samples of graphene on copper wires were characterized using Raman spectroscopy. Figure 25 shows the Raman peaks and peak intensity ratios of 2*D*-to *G*-peak of graphene grown copper wires. The peak intensity ratio confirmed the presence of 2-layer (2L) graphene on copper wires. The disappearance of the Raman peak after oxygen plasma treatment confirms that the graphene was removed successfully.

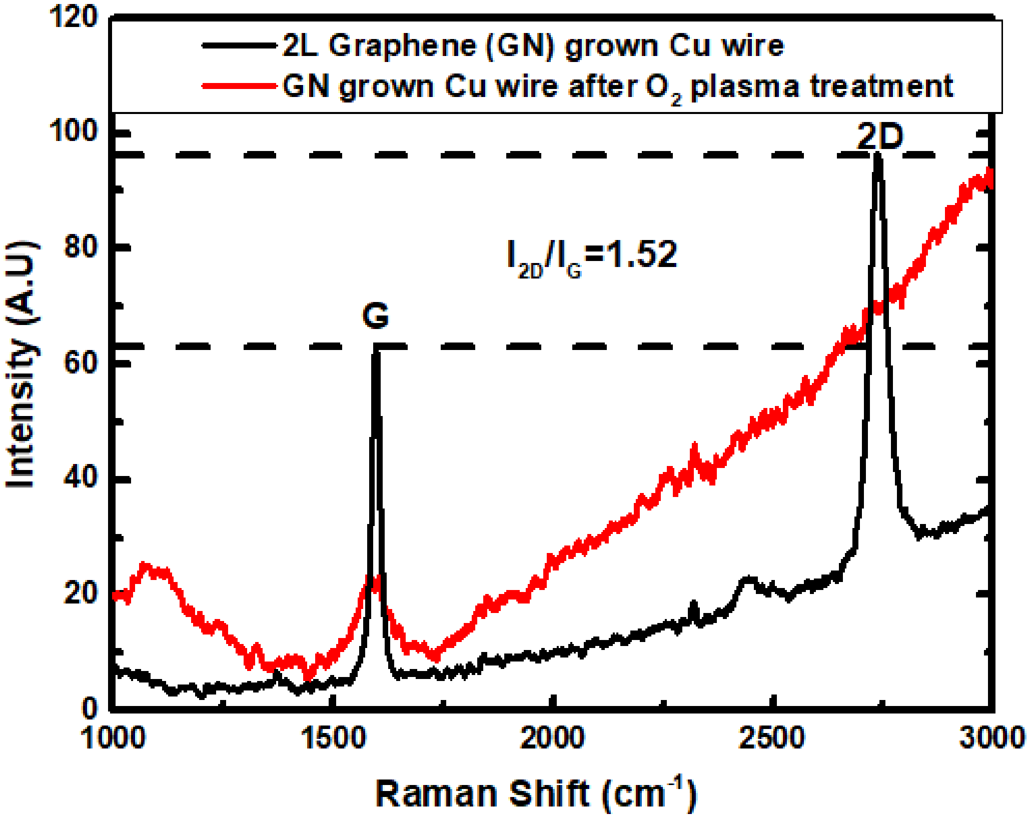

Figure 25: Raman spectra of graphene grown sample before (black) and after (red) oxygen plasma treatment.

Various treatments applied to the samples can potentially remove some of the sample material, changing its diameter. To avoid potential errors, the wire diameter was estimated both directly and using weight measurement. Figure 26 summarizes the diameter of various samples measured via the two approaches.

The results show that the weight measurement results are lower than the direct measurements. The decrease in wire diameter after plasma etching and annealing is due to material removal from the sample surface during those treatments. The larger difference between the two measurement values for the treated samples suggests that the surface material removal is not uniform. Similarly, the larger standard deviation for micrometer measurements confirms that wire diameter is not uniform along the measured length. Weight-based measurements might, therefore, be more a more accurate representation wire's average diameter.

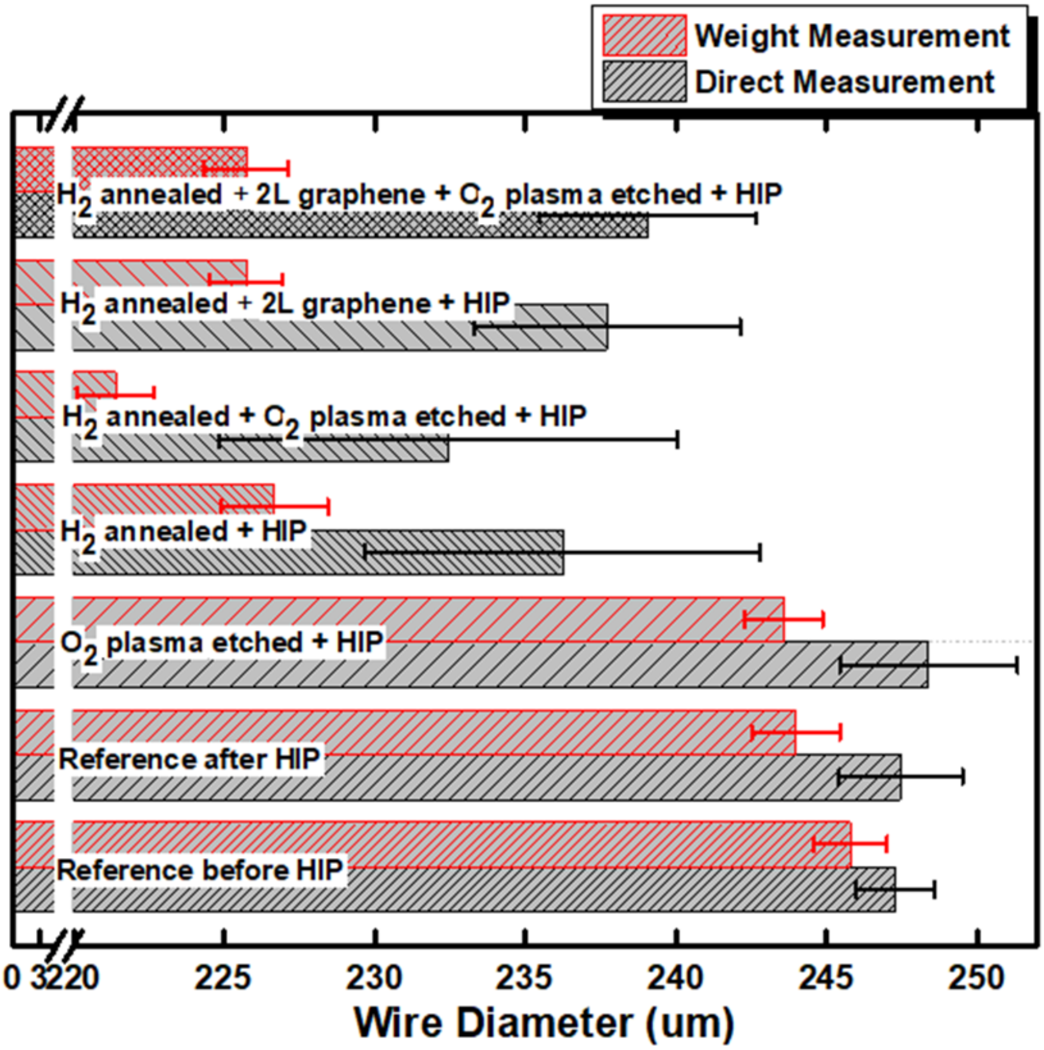

Figure 26: Wire diameter measurements using the weight method and direct micrometer measurements.

Figure *27* summarizes the electrical conductivity measurements of all specimens based on wire diameter measurements using both direct and weight measurement approaches. Conductivity values based on the weight measurement technique are close to 100% IACS. As discussed earlier, direct wire diameter measurements are not accurate and result in erroneous conductivity values. None of the treatments show any statistically meaningful improvement or reduction of electrical conductivity. Most importantly, with the graphene-grown copper wires and HIP, the electrical conductivity does not improve.

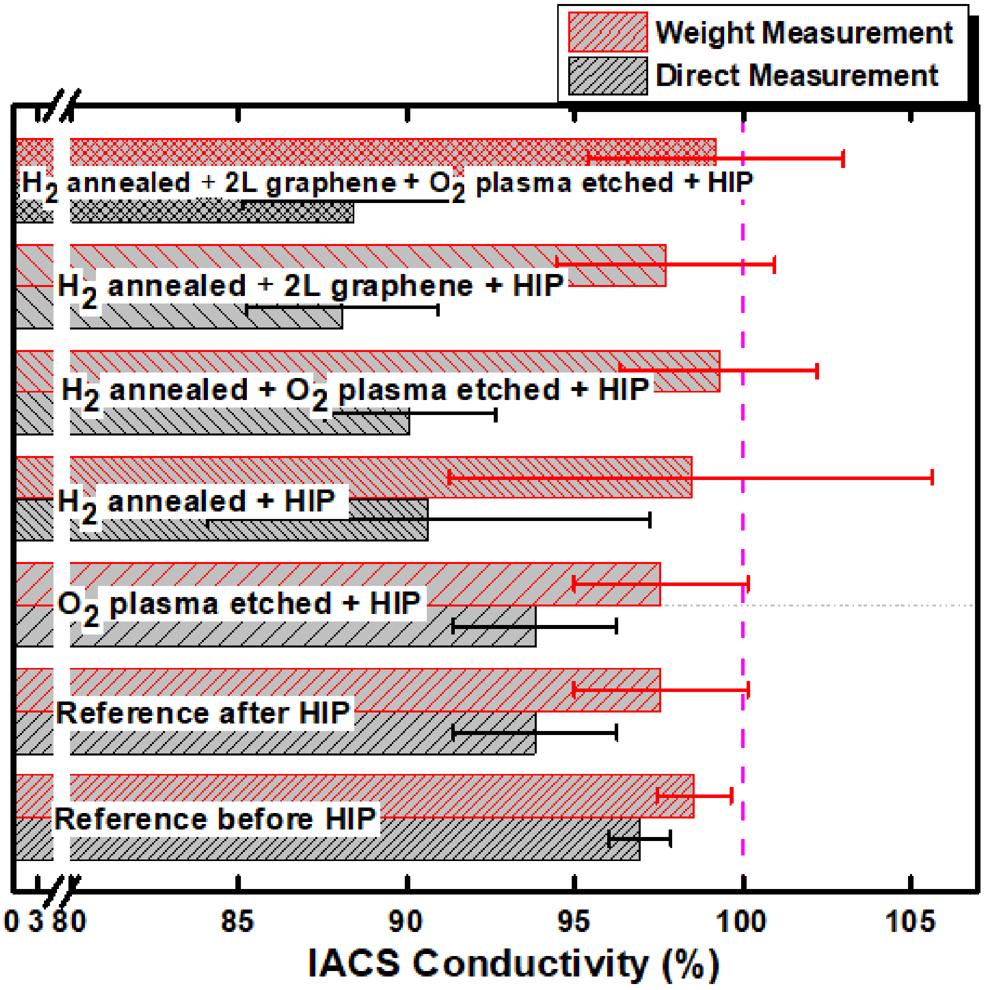

Figure 27: Electrical conductivity of various wire samples.

HIP and graphene growth alter the microstructure and surface of copper wires and are, therefore, expected to affect their current carrying capacity. The ampacity of wires, measured here in terms of the time it takes for the wire to break under a constant current for various samples in vacuum and air environments, is summarized in Figure 28. The reference non-HIP has a higher ampacity in the air than in vacuum. This is because the resistive heat generated in the wire is dissipated through convection, conduction, and radiation in the air but can only dissipate via radiation and conduction in vacuum. However, in all other cases, the wire in vacuum shows more than ~50% higher fusing times than in air. The treatments applied in this study, including HIP, degrade the sample surface quality and make the surface prone to diffusion and oxidation, resulting in an inferior performance. The surface defects (act as diffusion points) activate easier in the air than in the vacuum, which leads to early sample fusing in air.

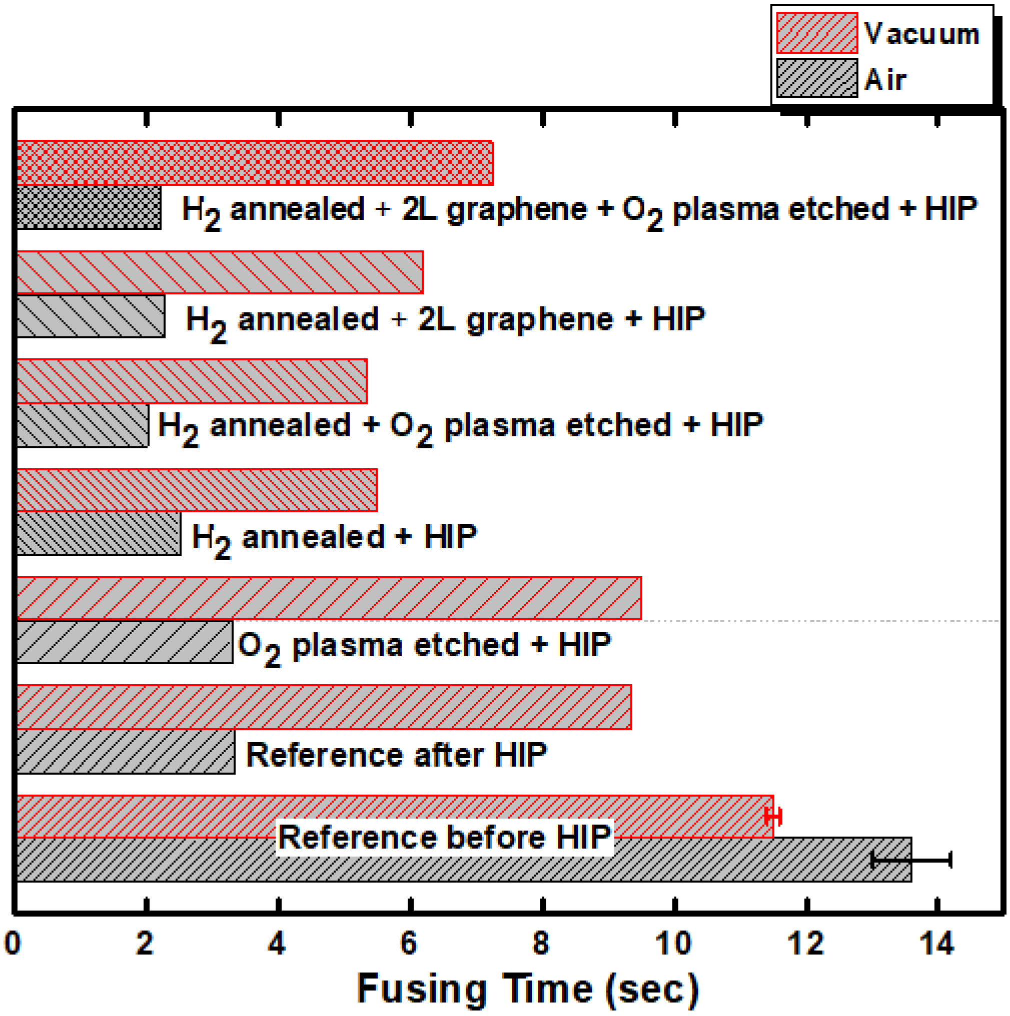

Figure 28: Ampacity of various wires in vacuum and air environments.

The temperature-dependent resistivity of samples was measured out from 298 to 423 °K (room to ~150 °C) at intervals of ~20 °K using the four-point probe method. The results in Figure 29 show the normalized resistance (by the room temperature resistance) for the reference copper wire (black) and the copper wire with a 2-layer

(2L) graphene grown on it (red). The temperature coefficient of resistance (TCR=dR/dT) is slightly (0.00375 vs. 0.00414) higher for the copper wire with graphene. Cleaning and hydrogen annealing is a prerequisite for good quality graphene growth. These steps, however, introduce some defects and non-uniformities, leading to an increase in electrical resistance at elevated temperatures compared with the reference copper wire.

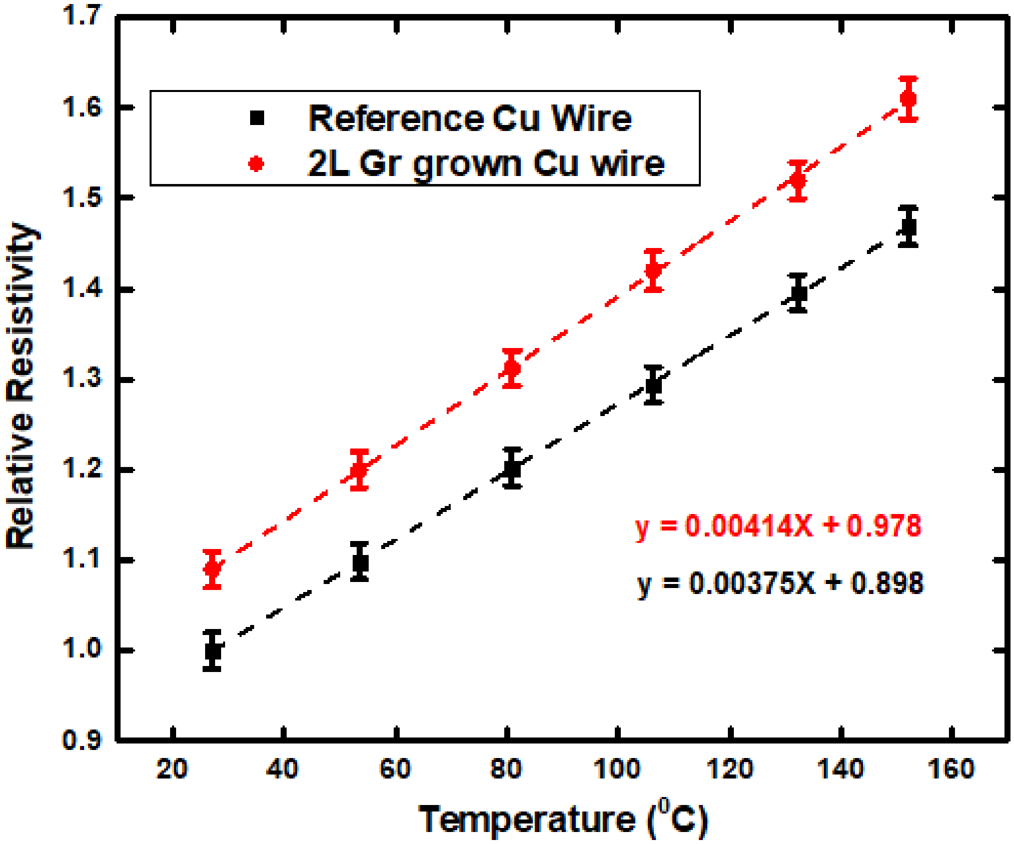

Figure 29: Electrical resistivity of the reference and 2L-graphene grown copper wire samples at elevated temperature.

Figure 30 shows the crystal orientations of copper specimens. Most of the grains are oriented in the (111) direction for the reference copper wire. The crystal orientation shifted between four different orientations, as shown in Figure 30, with the treatment conditions. However, the orientation changes mechanisms, either due to the treatment condition or sintering parameter or gas environment or graphene growth, which is unclear [91-96]. Grain growth at the elevated HIP temperatures might be responsible for the introduction of texture in wires.

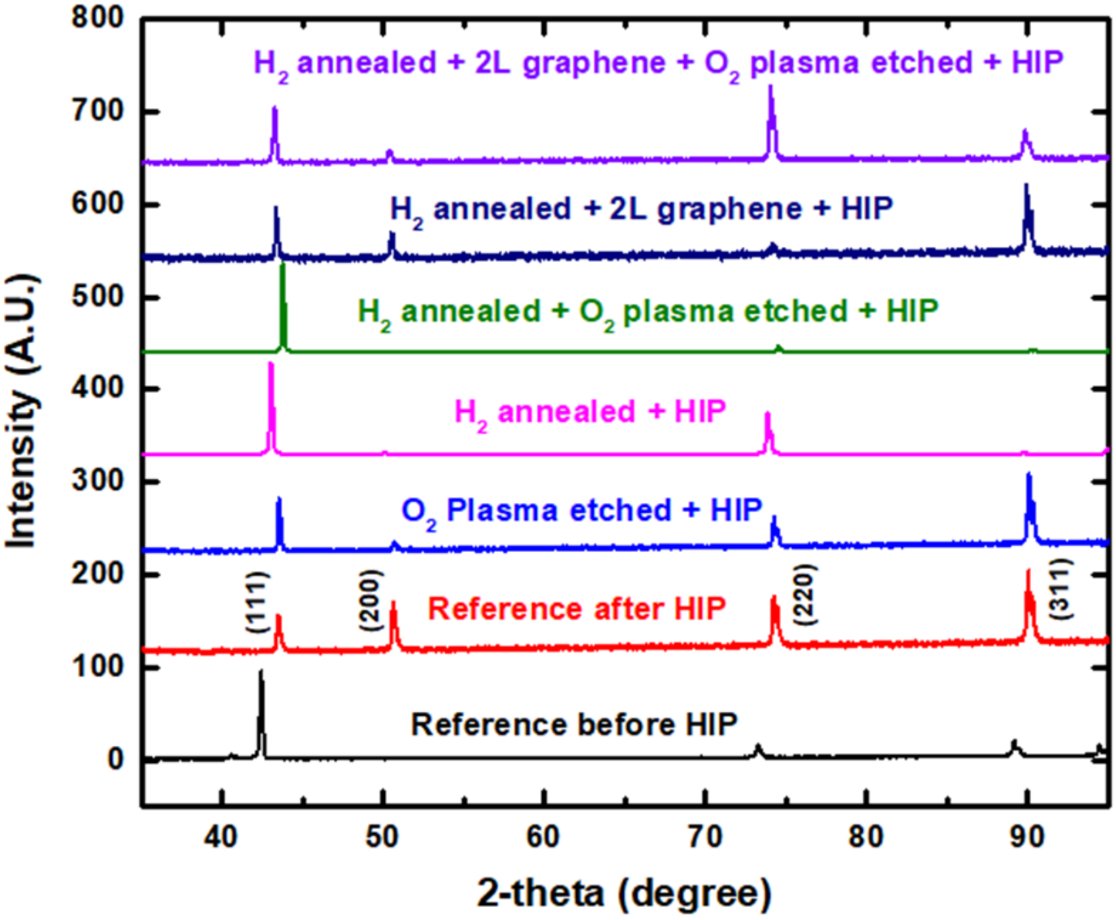

Figure 30: XRD of copper wires before and after various treatments.

Sample surfaces were investigated before and after the treatments. The treated sample surfaces appeared different, as shown in Figure 31, and contained more voids and defects after the treatments.

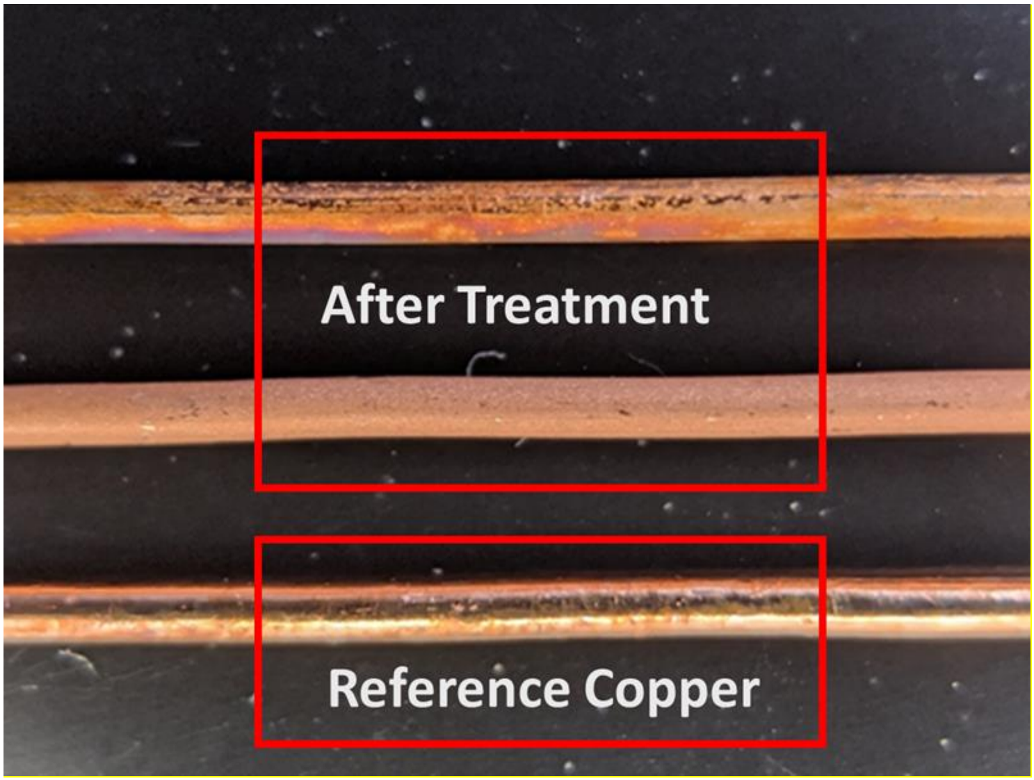

Figure 31: Sample surface of copper wires before and after the treatments.

4.4 Conclusions

Hot isostatic pressing and other surface treatments introduce surface defects to copper wires. The application of HIP brought insignificant changes to the conductivity and TCR of reference and graphene-grown copper wires. HIP introduced texture in copper wires. Despite other reports, the results presented in this chapter do not support any evidence of improved electrical properties by graphene growth or HIP treatments.

Chapter 5. Copper Carbon Matrix Processed in Molten Copper by Applying High Current

Raju Ghimire[1,2], Gehan C Jayatilaka[2], and Mehran Tehrani[2]

[1] Nanoscience and Microsystems Engineering, University of New Mexico, Albuquerque, NM, United States

[2] Department of Mechanical Engineering, The University of Texas at Austin, Austin, TX, United States

Abstract: Metal carbon interfaces have drawn much attention lately due to their unique physical and mechanical properties. There are reports of conversion of carbon sources in metal melts with the application of high electrical currents. These materials, called covetic, have shown some interesting yet unexplained properties. The formation of new structures as a result of covetic processing is still not well understood. This chapter investigates the possibility of forming new structures between copper and different carbon sources processed in molten copper by applying high currents. Properties of the carbon-copper interfaces were mapped using conductive atomic force microscopy (c-AFM), and carbon conversion was investigated using Raman spectroscopy.

5.1 Introduction

Fabrication of advanced electrical conductors that surpass conventionally used metals like aluminum, copper, and silver has gained increasing interest in critical applications like space flight, aviation, and energy. These applications usually demand higher electrical and thermal conductivity, superior mechanical properties, and lower specific weight. Incorporating various forms of carbon in metals can enhance their mechanical, thermal, and electrical properties [117, 121-124]. However, the solubility of carbon to most metals is low because of the inert nature of carbon [125, 126]. Solid-phase carbon nanoparticles are usually used [117, 121]. Shugart and Scherer discovered a new approach to making a single-phase metal-carbon material called "Covetics," which is gaining much attention nowadays [117, 127]. In the process, carbon is fused with metals, such as copper (Cu), aluminum (Al), and silver (Ag), with the aid of high electrical currents [128]. High current is applied during the process of mixing carbon in the molten metal, the purpose of which is to form single-phase metal-carbon material[127]. Bakir et al. claimed that the carbon nanofiller is covalently bonded to the host metal in Covetics [128]. Thus, in addition to enhanced electrical and thermal conductivity, covetics possess in situ generated interfacial bonding essential for improving mechanical properties [128].

Covetics of aluminum (Al), copper (Cu), and silver (Ag) with various amounts of carbon have been prepared and characterized since 2011 [128-130]. Brown et al. investigated the mechanical and electrical conductivity of 3wt.% carbon incorporated aluminum covetics [131]. No significant difference in the electrical conductivity between the neat aluminum and its covetic version was observed [131]. However, covetic aluminum's tensile strength and hardness were increased by 23% and 30%, respectively. Also, no variation in density was observed. Nilufar et al. prepared various aluminum covetics and reported that tensile strength and hardness for their Covetic samples were higher than pure aluminum by 43% and 5%, however, no change in modulus was found [129, 132]. Balachandran et al. studied the properties of 3 wt.% carbon content copper covetics and found enhancement in electrical and thermal conductivity by 7% and 10%, respectively [133]. The density of the control sample was the same as covetics in this study. Thus, to quantify the presence of carbon on covetics, Salamance et al. studied different metal covetics (Ag, Cu, and Al) and observed that carbon existed not only in "single-phase metal-carbon form" but also in the clustered form [134]. Carbon nanoparticles of size varying from 5nm to 200nm were detected though good electrical and thermal conductivity improvement was present [134]. Kareem et al. synthesized and characterized 3wt.% aluminum covetic and found the improvement of electrical conductivity by 34%, enhancement in tensile strength by 18%, hardness by 15%, and a notable density decrement of 6% compared to pure cast aluminum [135]. They concluded that the density and electrical conductivity of covetics depend on the voltage and direct current used during the fabrication process [135]. Jain et al. analyzed Raman spectra and EELS spectrum of Ag and Al covetics and found that there is mostly sp^2 bonding of C atom with a minor fraction of sp^3 bonds [136]. Recently, Ge et al. performed a systematic study on the effect of C- content on aluminum covetics and reported that the improvement in performance of Covetics is mainly because of high-quality interfaces between base metal (Al) and nano-crystalline graphitic structure [137]. Incorporation of Carbon via electro-charging-assisted process improved electrical conductivity by 6% and hardness by 8% compared to the pure base metal.

On the other hand, Knych et al. fabricated covetic copper wires with graphene through a cold drawing process from the cast. They measured the mechanical and electrical properties of the wire [138] and observed no change in tensile strength, elongation, and electrical conductivity of covetics compared to pure copper that was mainly due to the presence of a significant amount of impurities in the form of sulfur or iron [138]. Alongside, Degroh et al. at NASA investigated the morphology and the electrical conductivity of Cu Covetics with 0.4 wt.% of carbon content [127]. The controversial report with the existing result was achieved as the wire prepared from the covetic ingot possessed 9% lower electrical conductivity than similarly processed pure copper [127]. Knych et al. and Degroh et al. came to the same conclusion that the low conductivity of copper covetics is essentially due to the presence of impurities, voids, uneven distribution of carbon, and weak conducting interfaces created by C-lined voids [127, 138]. The quantification of carbon content remains a challenge for the covetics.

This study focuses on the synthesis and characterization of Copper Covetics in terms of their electrical conductivity with different forms of carbon. Copper is used in most electrical applications, such as wiring and power generation, because of its availability, cost, and electrical conductivity. Thus, any improvement in copper's conductivity would save billions of dollars in electricity bills. Various sources of carbon like graphene, multiwalled carbon nanotubes, graphite were used between the film of copper. An electrical sintering process called spark plasma sintering was used to prepare the copper covetics. AFM, Raman, SEM, FTIR was performed as a means characterization.

5.2 Experimental Methods

Copper foils (99.99% pure) from Sigma Aldrich were used as a host material. Various carbon materials are used as a carbon additive. Four different carbon sources were used: graphene sheet from Graphene Supermarket, graphite synthetic powder from Sigma Aldrich, self-prepared graphene oxide (GO) sheet, and carbon nanotube tape (CNT) Tape from DexMat.

A spark plasma sintering (SPS) device was used to fabricate the samples. SPS is a pressure-assisted pulsed-current process in which the samples are loaded in an electrically conducting die and sintered under uniaxial pressure. When a direct current (DC) passes through the die, it heats both the die and sample. The sample can, therefore, be heated from different directions, leading to fast heating and rapid consolidation [139].

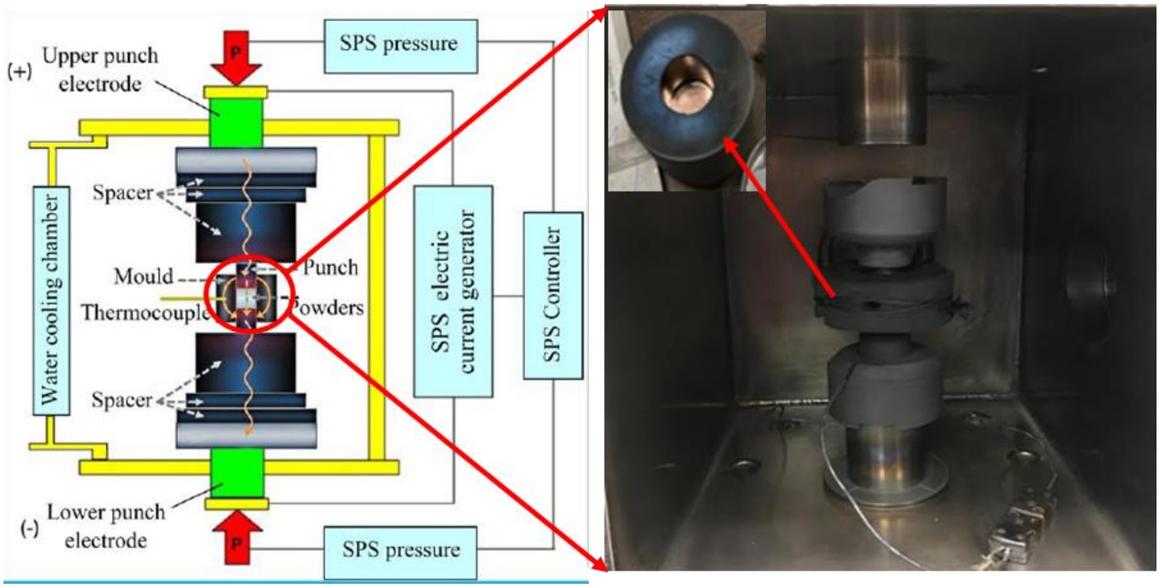

Figure 32: Schematic and actual Spark Plasma Sintering (SPS) setup.

Each specimen, containing a carbon source stacked between two copper foils, was loaded into the die between two punch electrodes. A high current was applied to reach ~1350 °C while applying a uniaxial default pressure of 1 MPa. The applied heating rate was ~60 °C per minute, and a pyrometer monitored the temperature. The experiment was conducted in a nominal vacuum (mTorr) environment. Cross-sectional samples with each carbon source perpendicular to the cut direction were prepared for further characterization. The samples were mounted in an acrylic mold, ground using sandpaper up to a maximum grit of 2400, and finally 3 μm diamond suspension was used to polish the samples.

The electrical properties along and across the sample interface area were mapped using the contact mode of conductive atomic force microscopy (c-AFM, Park NX10) by applying the bias between the tip and the sample. For the measurement, one side of the copper carbon composite sample was attached and electrically connected to the sample holder using double-sided conductive carbon tape. At the same time, a Pt coated Si-cantilever with the measuring voltage applied was swept over the polished surface on the other side of the sample. An FEI Quanta 650 scanning electron microscopy was used to investigate samples' microstructures.

5.3 Results and Discussion

The interfacial bonding between copper and graphene sheet was investigated by processing them at different temperatures and pressures while keeping the holding time constant. Results show that the effect of temperature was dominant over applied pressure to improve the interfacial bonding. The sample processed at temperature 950 °C and 50 MPa uniaxial pressure (Figure 33B) shows that the voids appear throughout the interface, limiting the interfacial properties. On the other hand, the same sample processed at temperature 1350 °C and 1 MPa uniaxial pressure (Figure 33C) shows that the bonding between copper and graphene sheets improved, and all the interfacial voids disappeared. To final set of samples (Figure 33(1) to Figure 33(4)) processed at temperature 1350 °C and 1 MPa uniaxial pressure shows good interfacial bonding without voids.

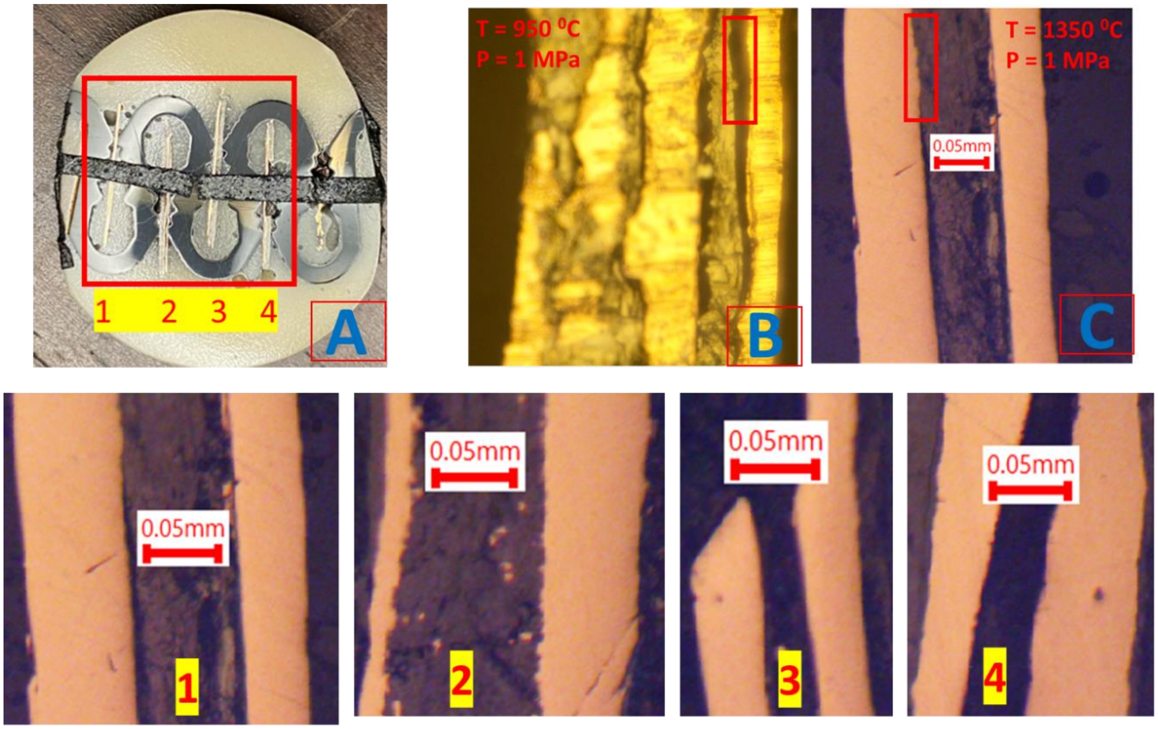

Figure 33: Covetic sample preparation and parameter optimization: (A) All polished samples in a mold, (B and C) Copper and graphene sheet processed at different temperatures and pressure, (1-4) Copper processed with graphene sheet, graphene powder, graphene oxide sheet, and carbon nanotube tape at 1350 °C and 1MPa temperature and pressure respectively.

A comparison of current flow for four different samples was obtained using the C-AFM mapping method as described above. Figure 34 and Figure 35 show that the maximum current flows through the carbon side for all the samples except the sample with carbon nanotube tape. However, in the case of copper and graphene powder sample, in

Figure 35, the current flow mapping is almost similar throughout the scan area. However, the graphene powder has diffused into the copper (see Figure

33(2)), resulting in high current flows around the copper-carbon interface. It is not understood that the reason to have the higher current on the carbon side rather than the copper side during c-AFM current mapping.

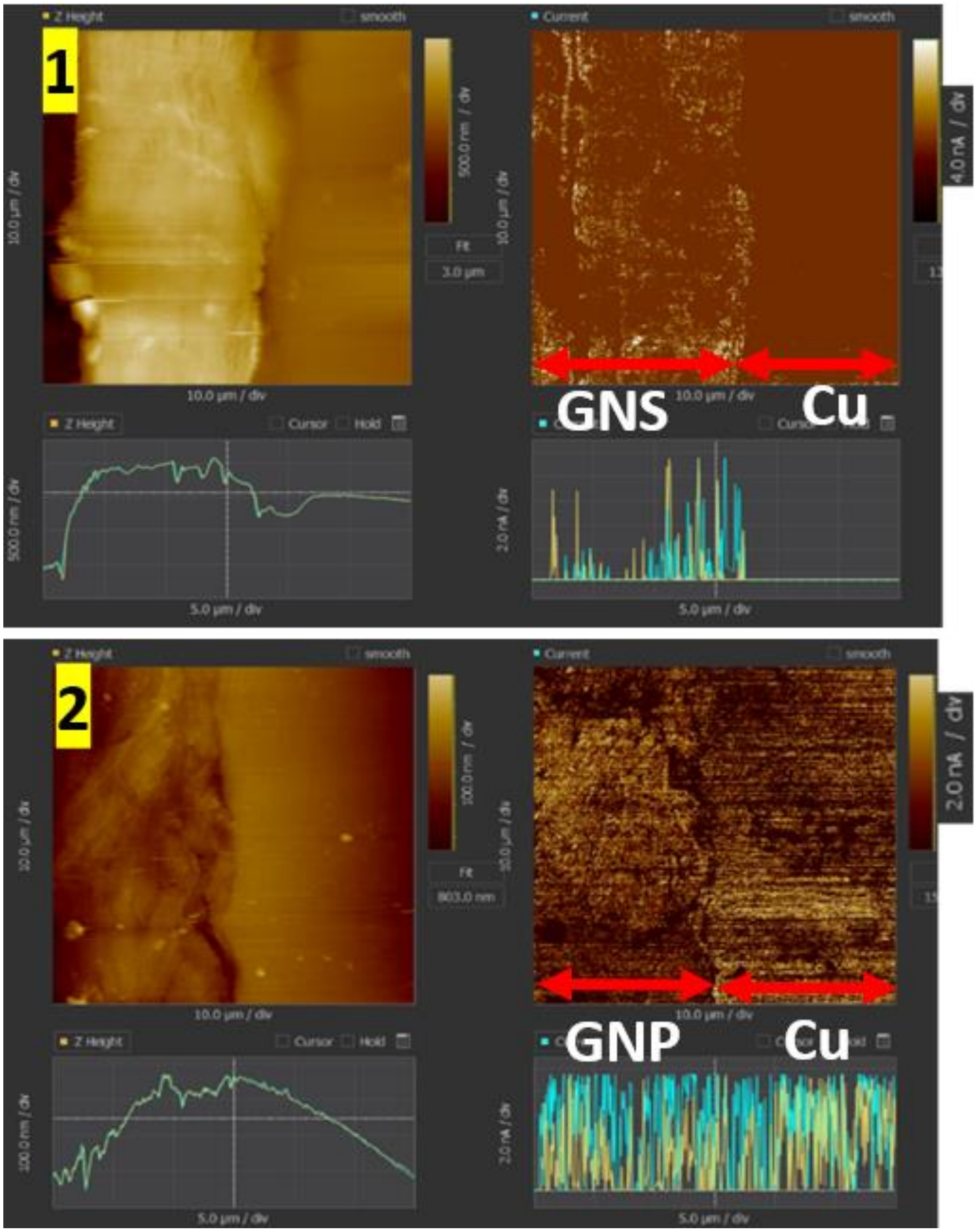

Figure 34: Current mapping image of copper with (1) graphene sheet and (2) graphene powder.

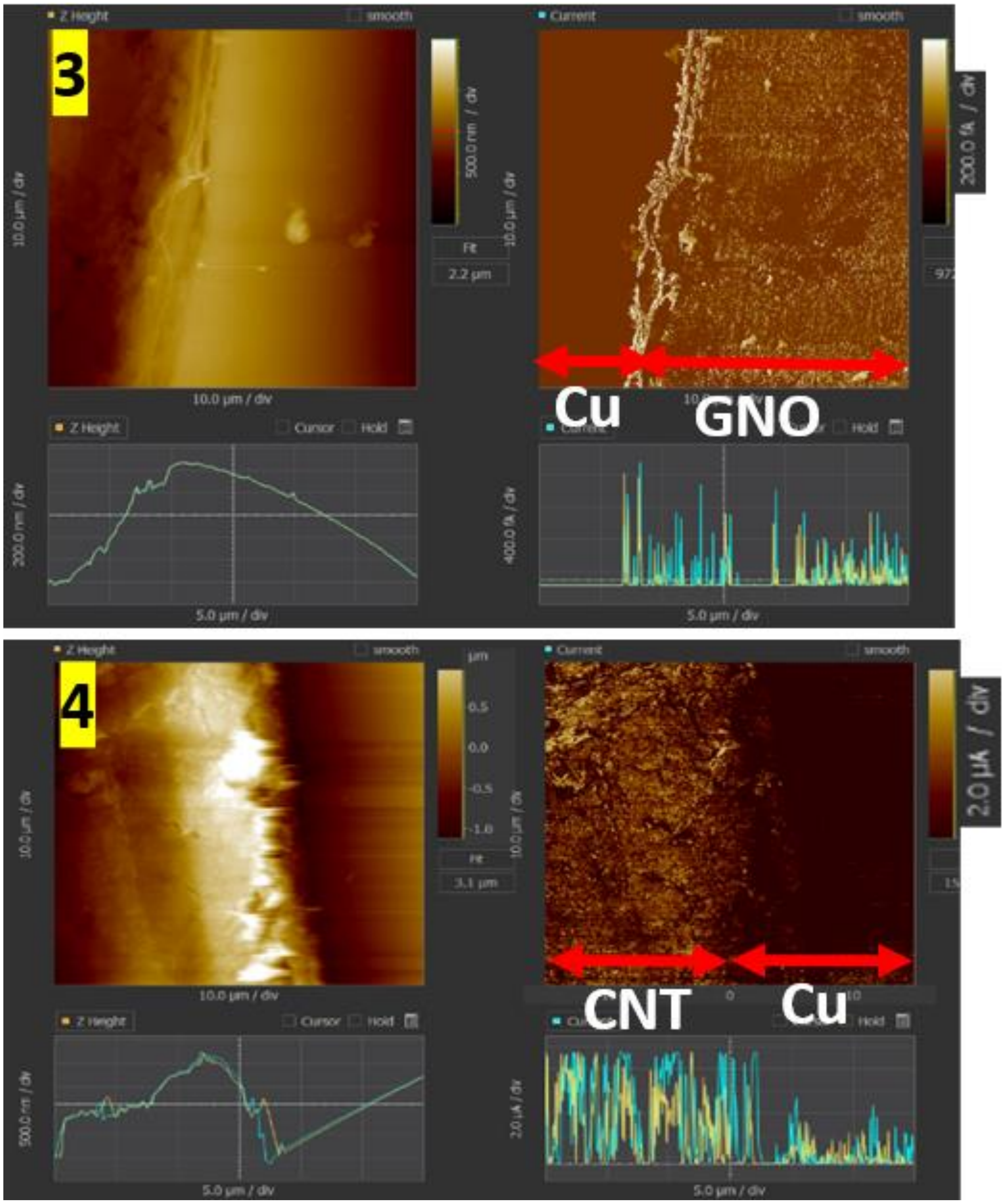

Figure 35: Current mapping image of copper with (3) graphene oxide sheet, (4) carbon nanotube tape.

Figure 36 shows the SEM images of copper carbon interfaces after the “covetic” treatment. Some copper particles appear on the carbon side, which is due to the migration of molten copper during such treatment. However, there is no evidence of the formation of Covetics or other unique interfacial structures, similar to those reported in the literature.

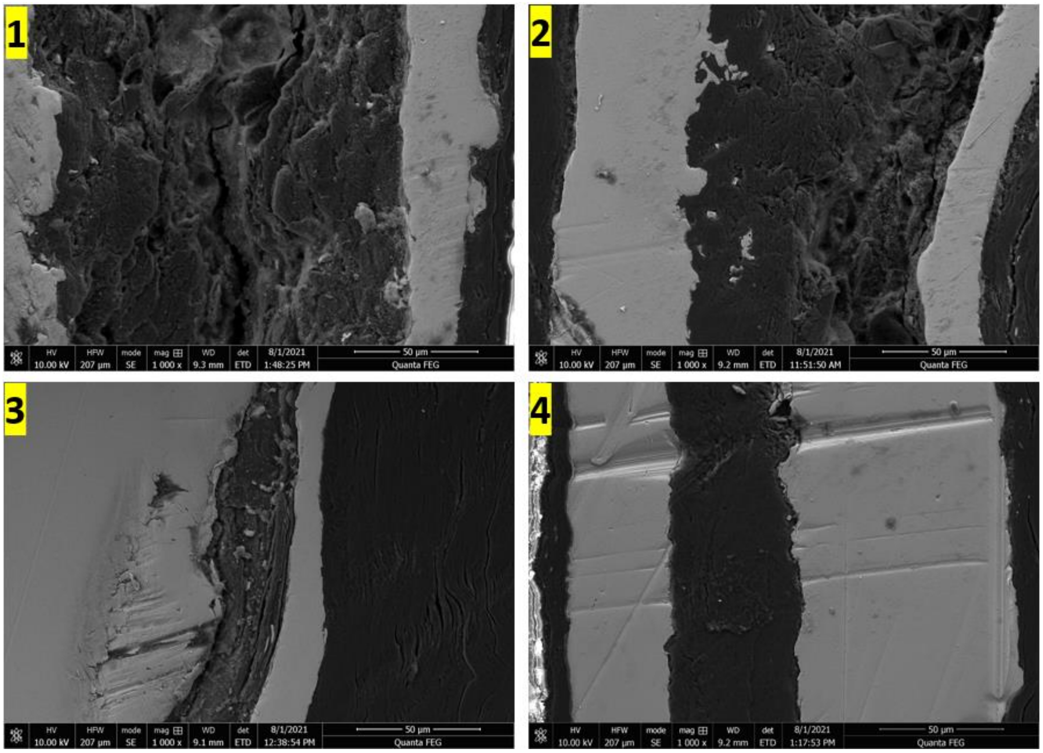

Figure 36: SEM image of the interface of copper with four different carbon sources: (1) graphene sheet, (2) graphene powder, (3) graphene oxide sheet, (4) carbon nanotube tape.

5.4 Conclusions

High electrical current processing above copper’s melting temperature was used to prepare carbon-copper samples. The appearance of higher current on carbonaceous regions on carbon-copper interfaces, during c-AFM current mapping, is not well understood. This may be due to the nature of c-AFM measurements. SEM images do not show any evidence of Covetics formation.

Chapter 6. Conclusions and Future Work

This dissertation investigates the different aspects of advanced GN-Cu conductors. In particular, it improves our understanding of advanced electrical conductors using classical modeling, atomistic simulation, and experimentation. The experimental part includes the synthesis, fabrication, and characterization of GN-Cu multilayered films and extreme processing under high currents. Most importantly, this work sheds light on the importance of error analysis and measurement techniques for conductivity measurements, especially for thin-film specimens. The body of research here dissects some controversial reports in the field of graphene copper advanced conductors and provides explanations to prevent future research from possible misdirection.

The combined quantum-classical calculations show that graphene sandwiched between copper layers can accept electrons from copper and contribute to the overall conductivity if it can achieve mobilities higher than freestanding graphene. This means that graphene or the interface between graphene and copper should achieve ultrahigh electron mobility even at high electron densities.

Thickness measurement errors, measured via standard micrometers, introduce large variations in electrical conductivity of thin foil samples (<50um), and as the samples become thicker (>100um), the effect of measurement errors becomes smaller. We demonstrated the importance of proper error analysis and choice of measurement technique for thin conductor foils. Our results show that all measurement values should be reported with their associated error values calculated from uncertainty propagation analysis. The performance of GN-Cu samples from 300-400K is improved by 3.1% over pure copper due to the developed texture in the samples. However, graphene didn't enhance conductivity in the studied samples. DFT results show that in the GN-Cu composite the $3pz$-states of graphene are strongly mixed with $3d$-states of copper, providing a non-zero density of electronic states at Dirac point. Additionally, the Fermi energy of graphene is pushed to higher values resulting in *n*-doping of graphene. Results also showed that the majority of electrons can get trapped at the interfaces and could move along the interfaces, potentially with ultrahigh mobilities.

Hot isostatic pressing and other surface treatments introduce surface defects to copper wires. The application of HIP brought insignificant changes to the conductivity and TCR of reference and graphene-grown copper wires. HIP introduced a new texture in copper wires. Despite other reports, the results presented in this dissertation do not support any evidence of improved electrical properties by graphene growth or HIP treatments.

High electrical current processing above copper's melting temperature was used to prepare carbon-copper samples. The appearance of higher current on carbonaceous regions on carbon-copper interfaces, during c-AFM current mapping, is not well understood. This may be due to the nature of c-AFM measurements. SEM images do not show any evidence of Covetics formation.

Besides the findings of this dissertation, this work has generated some fundamentally interesting questions for the advanced conductor community, such as 1) does graphene sandwiched between metals or graphene-metal interface have ultrahigh electron mobility even at extremely high electron densities? 2) Why does c-AFM mapping show higher currents on carbonaceous regions and lower on copper? 3) do covetics form, and if so, how?

References

1. Tehrani, M., *Advanced Electrical Conductors: An Overview and Prospects of Metal Nanocomposite and Nanocarbon Based Conductors.* arXiv preprint arXiv:2011.03090, 2020.
2. Sundaram, R.M., et al., *Copper/carbon nanotube composites: research trends and outlook.* R Soc Open Sci, 2018. **5**(11): p. 180814.
3. Subramaniam, C., et al., *One hundred fold increase in current carrying capacity in a carbon nanotube–copper composite.* 2013. **4**: p. 2202.
4. Nazeer, F., et al., *Effect of processing routes on mechanical and thermal properties of copper-graphene composites.* Materials Science and Technology, 2019. **35**(14): p. 1770-1774.
5. Nazeer, F., et al., *Thermal and mechanical properties of copper-graphite and copper-reduced graphene oxide composites.* Composites Part B-Engineering, 2019. **163**: p. 77-85.
6. Gao, X., et al., *Mechanical properties and thermal conductivity of graphene reinforced copper matrix composites.* Powder Technology, 2016. **301**: p. 601-607.
7. Chen, F.Y., et al., *Effects of graphene content on the microstructure and properties of copper matrix composites.* Carbon, 2016. **96**: p. 836-842.
8. Cao, M., et al., *Ultrahigh Electrical Conductivity of Graphene Embedded in Metals.* Advanced Functional Materials, 2019. **29**(17).
9. Kappagantula, K., X. Li, and G. Grant, *Direct Extruded High Conductivity Copper for Electric Machines, Materials 2019 Annual Progress Report*. 2019: Washington DC.
10. Tehrani, M., *Advanced Electrical Conductors: An Overview and Prospects of Metal Nanocomposite and Nanocarbon Based Conductors.* physica status solidi (a), 2021. **218**(8): p. 2000704.
11. Cao, M., et al., *Ultrahigh electrical conductivity of graphene embedded in metals.* Advanced Functional Materials, 2019. **29**(17): p. 1806792.
12. Cai, S., et al., *Fabrication of Three-Dimensional Graphene/Cu-Ag Composites by In Situ Chemical Vapor Deposition and Their Properties.* Journal of Materials Engineering and Performance, 2020: p. 1-8.
13. Cao, M., et al., *The influence of interface structure on the electrical conductivity of graphene embedded in aluminum matrix.* Advanced Materials Interfaces, 2019. **6**(13): p. 1900468.
14. Smith, J.A., *Electrical Performance of Copper-Graphene Nano-Alloys*. 2019, Ohio University.
15. Tezura, M. and T. Kizuka, *Crossing interfacial conduction in nanometer-sized graphitic carbon layers.* Nanoscale Horizons, 2020.
16. Yang, M., et al., *Metal-graphene interfaces in epitaxial and bulk systems: A review.* Progress in Materials Science, 2020. **110**: p. 100652.
17. Di Bartolomeo, A., *Graphene Schottky diodes: An experimental review of the rectifying graphene/semiconductor heterojunction.* Physics Reports, 2016. **606**: p. 1-58.

18. Barraza-Lopez, S., et al., *Effects of metallic contacts on electron transport through graphene.* Physical review letters, 2010. **104**(7): p. 076807.

19. Cayssol, J., B. Huard, and D. Goldhaber-Gordon, *Contact resistance and shot noise in graphene transistors.* Physical Review B, 2009. **79**(7): p. 075428.

20. Maassen, J., W. Ji, and H. Guo, *First principles study of electronic transport through a Cu (111)/graphene junction.* Applied Physics Letters, 2010. **97**(14): p. 142105.

21. Xia, F., et al., *The origins and limits of metal–graphene junction resistance.* Nature nanotechnology, 2011. **6**(3): p. 179.

22. Nouchi, R. and K. Tanigaki, *Competitive interfacial charge transfer to graphene from the electrode contacts and surface adsorbates.* Applied Physics Letters, 2015. **106**(8): p. 083107.

23. Giovannetti, G., et al., *Doping graphene with metal contacts.* Physical review letters, 2008. **101**(2): p. 026803.

24. Gong, C., et al., *First-principles study of metal–graphene interfaces.* Journal of Applied Physics, 2010. **108**(12): p. 123711.

25. Matsuda, Y., W.-Q. Deng, and W.A. Goddard, *Contact resistance properties between nanotubes and various metals from quantum mechanics.* The Journal of Physical Chemistry C, 2007. **111**(29): p. 11113-11116.

26. Dahal, A. and M. Batzill, *Graphene-nickel interfaces: a review.* Nanoscale, 2014. **6**(5): p. 2548-62.

27. Gong, C., et al., *Metal–graphene–metal sandwich contacts for enhanced interface bonding and work function control.* ACS nano, 2012. **6**(6): p. 5381-5387.

28. Dahal, A. and M. Batzill, *Graphene–nickel interfaces: a review.* Nanoscale, 2014. **6**(5): p. 2548-2562.

29. Klein, C., D. Cohen-Elias, and G. Sarusi, *Controlling graphene work function by doping in a MOCVD reactor.* Heliyon, 2018. **4**(12): p. e01030.

30. Song, S.M., et al., *Determination of work function of graphene under a metal electrode and its role in contact resistance.* Nano letters, 2012. **12**(8): p. 3887-3892.

31. Yu, Y.-J., et al., *Tuning the graphene work function by electric field effect.* Nano letters, 2009. **9**(10): p. 3430-3434.

32. Goli, P., et al., *Thermal properties of graphene–copper–graphene heterogeneous films.* Nano letters, 2014. **14**(3): p. 1497-1503.

33. Kwon, K.C., K.S. Choi, and S.Y. Kim, *Increased work function in few-layer graphene sheets via metal chloride doping.* Advanced Functional Materials, 2012. **22**(22): p. 4724-4731.

34. Li, W. and D. Li, *On the correlation between surface roughness and work function in copper.* The Journal of chemical physics, 2005. **122**(6): p. 064708.

35. Lin, Y., et al., *Graphene/semiconductor heterojunction solar cells with modulated antireflection and graphene work function.* Energy & Environmental Science, 2013. **6**(1): p. 108-115.

36. Siokou, A., et al., *Surface refinement and electronic properties of graphene layers grown on copper substrate: an XPS, UPS and EELS study.* Applied Surface Science, 2011. **257**(23): p. 9785-9790.

37. Zhu, F., et al., *Heating graphene to incandescence and the measurement of its work function by the thermionic emission method.* Nano Research, 2014. **7**(4): p. 553-560.

38. Abergel, D., et al., *Properties of graphene: a theoretical perspective.* Advances in Physics, 2010. **59**(4): p. 261-482.

39. Kholmanov, I.N., et al., *Improved electrical conductivity of graphene films integrated with metal nanowires.* Nano letters, 2012. **12**(11): p. 5679-5683.

40. Klimchitskaya, G. and V. Mostepanenko, *Conductivity of pure graphene: Theoretical approach using the polarization tensor.* Physical Review B, 2016. **93**(24): p. 245419.

41. Ma, T., et al., *Tailoring the thermal and electrical transport properties of graphene films by grain size engineering.* Nature communications, 2017. **8**(1): p. 1-9.

42. Sang, M., et al., *Electronic and thermal properties of graphene and recent advances in graphene based electronics applications.* Nanomaterials, 2019. **9**(3): p. 374.

43. Worsley, M.A., et al., *Mechanically robust 3D graphene macroassembly with high surface area.* Chemical Communications, 2012. **48**(67): p. 8428-8430.

44. Worsley, M.A., et al., *Synthesis of graphene aerogel with high electrical conductivity.* Journal of the American Chemical Society, 2010. **132**(40): p. 14067-14069.

45. Cao, M., et al., *Aligning graphene in bulk copper: Nacre-inspired nanolaminated architecture coupled with in-situ processing for enhanced mechanical properties and high electrical conductivity.* Carbon, 2017. **117**: p. 65-74.

46. Daneshvar, F., et al., *Fabrication of Light-Weight and Highly Conductive Copper–Carbon Nanotube Core–Shell Fibers Through Interface Design.* Advanced Materials Interfaces, 2020: p. 2000779.

47. Hidalgo-Manrique, P., et al., *Copper/graphene composites: a review.* Journal of materials science, 2019: p. 1-54.

48. Lu, L., et al., *Ultrahigh strength and high electrical conductivity in copper.* Science, 2004. **304**(5669): p. 422-426.

49. Cavallucci, T., et al., *Morphing graphene-based systems for applications: perspectives from simulations*, in *GraphITA*. 2017, Springer. p. 87-111.

50. Förster, G.D., *Atomistic modeling of metallic nanoparticles on carbonaceous substrates and epitaxial graphene on metals*. 2015.

51. Liu, X., et al., *Growth morphology and properties of metals on graphene.* Progress in Surface Science, 2015. **90**(4): p. 397-443.

52. Safina, L.R., J.A. Baimova, and R.R. Mulyukov, *Nickel nanoparticles inside carbon nanostructures: atomistic simulation.* Mechanics of Advanced Materials and Modern Processes, 2019. **5**(1): p. 1-11.

53. Xu, Z., et al., *Large scale atomistic simulation of single-layer graphene growth on Ni (111) surface: molecular dynamics simulation based on a new generation of carbon–metal potential.* Nanoscale, 2016. **8**(2): p. 921-929.

54. Mohsin, K., et al., *Current transport in graphene/copper hybrid nano ribbon interconnect: A first principle study.* ECS Transactions, 2016. **75**(13): p. 49.

55. Akturk, A. and N. Goldsman, *Electron transport and full-band electron-phonon interactions in graphene.* Journal of Applied Physics, 2008. **103**(5): p. 053702.

56. Chen, J.-H., et al., *Intrinsic and extrinsic performance limits of graphene devices on SiO 2.* Nature nanotechnology, 2008. **3**(4): p. 206.

57. Tran, N.T.T., et al., *Geometric and electronic properties of graphene-related systems: Chemical bonding schemes*. 2017: CRC Press.

58. Banszerus, L., et al., *Ultrahigh-mobility graphene devices from chemical vapor deposition on reusable copper.* Science advances, 2015. **1**(6): p. e1500222.

59. Cooper, D.R., et al., *Experimental review of graphene.* ISRN Condensed Matter Physics, 2012. **2012**.

60. Khomyakov, P., et al., *First-principles study of the interaction and charge transfer between graphene and metals.* Physical Review B, 2009. **79**(19): p. 195425.

61. Horng, J., et al., *Drude conductivity of Dirac fermions in graphene.* Physical Review B, 2011. **83**(16): p. 165113.

62. Giovannetti, G., et al., *Doping graphene with metal contacts.* Physical review letters, 2008. **101**(2): p. 026803.

63. Ajmal, M., et al., *Fabrication of the best conductor from single-crystal copper and the contribution of grain boundaries to the Debye temperature.* CrystEngComm, 2012. **14**(4): p. 1463-1467.

64. Cho, Y.C., et al., *Copper better than silver: electrical resistivity of the grain-free single-crystal copper wire.* Crystal growth & design, 2010. **10**(6): p. 2780-2784.

65. Bolotin, K.I., et al., *Ultrahigh electron mobility in suspended graphene.* Solid state communications, 2008. **146**(9-10): p. 351-355.

66. Neugebauer, P., et al., *How perfect can graphene be?* Physical review letters, 2009. **103**(13): p. 136403.

67. Banszerus, L., et al., *Extraordinary high room-temperature carrier mobility in graphene-WSe $ _2 $ heterostructures.* arXiv preprint arXiv:1909.09523, 2019.

68. Hwang, E.H. and S. Das Sarma, *Acoustic phonon scattering limited carrier mobility in two-dimensional extrinsic graphene.* Physical Review B, 2008. **77**(11): p. 115449.

69. Sohier, T., et al., *Phonon-limited resistivity of graphene by first-principles calculations: Electron-phonon interactions, strain-induced gauge field, and Boltzmann equation.* Physical Review B, 2014. **90**(12): p. 125414.

70. Wang, X., et al. *Characterization of Graphene/Cu Composites Prepared by CVD and SPS*. in *Chinese Materials Conference*. 2018. Springer.

71. Tjong, S.C., *Recent progress in the development and properties of novel metal matrix nanocomposites reinforced with carbon nanotubes and graphene nanosheets.* Materials Science and Engineering: R: Reports, 2013. **74**(10): p. 281-350.

72. Behabtu, N., et al., *Strong, light, multifunctional fibers of carbon nanotubes with ultrahigh conductivity.* science, 2013. **339**(6116): p. 182-186.

73. Milowska, K.Z., et al., *Carbon nanotube functionalization as a route to enhancing the electrical and mechanical properties of Cu–CNT composites.* Nanoscale, 2019. **11**(1): p. 145-157.

74. Akbarpour, M., et al., *Mechanical, tribological and electrical properties of Cu-CNT composites fabricated by flake powder metallurgy method.* Archives of Civil and Mechanical Engineering, 2019. **19**: p. 694-706.

75. Lekawa-Raus, A., et al., *Electrical properties of carbon nanotube based fibers and their future use in electrical wiring.* Advanced Functional Materials, 2014. **24**(24): p. 3661-3682.

76. Sundaram, R., et al., *Electrical performance of lightweight CNT-Cu composite wires impacted by surface and internal Cu spatial distribution.* Scientific reports, 2017. **7**(1): p. 1-11.

77. Subramaniam, C., et al., *Nano-scale, planar and multi-tiered current pathways from a carbon nanotube–copper composite with high conductivity, ampacity and stability.* Nanoscale, 2016. **8**(7): p. 3888-3894.

78. Chen, Y., et al., *Fabrication of in-situ grown graphene reinforced Cu matrix composites.* Scientific reports, 2016. **6**: p. 19363.

79. Ferrari, A.C., et al., *Science and technology roadmap for graphene, related two-dimensional crystals, and hybrid systems.* Nanoscale, 2015. **7**(11): p. 4598-4810.

80. Kim, Y., et al., *Strengthening effect of single-atomic-layer graphene in metal–graphene nanolayered composites.* Nature communications, 2013. **4**(1): p. 1-7.

81. Wang, S., et al., *High-quality graphene directly grown on Cu nanoparticles for Cu-graphene nanocomposites.* Materials & Design, 2018. **139**: p. 181-187.

82. Xiong, D.-B., et al., *Graphene-and-copper artificial nacre fabricated by a preform impregnation process: bioinspired strategy for strengthening-toughening of metal matrix composite.* Acs Nano, 2015. **9**(7): p. 6934-6943.

83. Kim, J.Y., et al., *Abnormal drop in electrical resistivity with impurity doping of single-crystal Ag.* Scientific reports, 2014. **4**(1): p. 1-5.

84. Miccoli, I., et al., *The 100th anniversary of the four-point probe technique: the role of probe geometries in isotropic and anisotropic systems.* Journal of Physics: Condensed Matter, 2015. **27**(22): p. 223201.

85. Fuentes-Cabrera, M., et al., *Bridge structure for the graphene/Ni (111) system: a first principles study.* Physical Review B, 2008. **77**(3): p. 035405.

86. Kresse, G. and J. Furthmüller, *Efficiency of ab-initio total energy calculations for metals and semiconductors using a plane-wave basis set.* Computational materials science, 1996. **6**(1): p. 15-50.

87. Kresse, G. and J. Furthmüller, *Efficient iterative schemes for ab initio total-energy calculations using a plane-wave basis set.* Physical review B, 1996. **54**(16): p. 11169.

88. Kresse, G. and J. Hafner, *Ab initio molecular dynamics for liquid metals.* Physical review B, 1993. **47**(1): p. 558.

89. Kresse, G. and J. Hafner, *Ab initio molecular-dynamics simulation of the liquid-metal–amorphous-semiconductor transition in germanium.* Physical Review B, 1994. **49**(20): p. 14251.

90. JCGM, J., *Evaluation of measurement data—Guide to the expression of uncertainty in measurement.* Int. Organ. Stand. Geneva ISBN, 2008. **50**: p. 134.

91. Hu, J., et al., *Roles of oxygen and hydrogen in crystal orientation transition of copper foils for high-quality graphene growth.* Scientific reports, 2017. **7**: p. 45358.

92. Jin, S., et al., *Colossal grain growth yields single-crystal metal foils by contact-free annealing.* Science, 2018. **362**(6418): p. 1021-1025.

93. Lee, S., et al., *Fabrication of high-quality single-crystal Cu thin films using radio-frequency sputtering.* Scientific reports, 2014. **4**: p. 6230.

94. Mudiyanselage, K., et al., *Adsorption of hydrogen on the surface and sub-surface of Cu (111).* The Journal of Chemical Physics, 2013. **139**(4): p. 044712.

95. Wu, M., et al., *Seeded growth of large single-crystal copper foils with high-index facets.* Nature, 2020. **581**(7809): p. 406-410.

96. Zhilyaev, A.P., S.N. Sergeev, and T.G. Langdon, *Electron backscatter diffraction (EBSD) microstructure evolution in HPT copper annealed at a low temperature.* Journal of Materials Research and Technology, 2014. **3**(4): p. 338-343.

97. Xu, Z. and M.J. Buehler, *Interface structure and mechanics between graphene and metal substrates: a first-principles study.* Journal of Physics: Condensed Matter, 2010. **22**(48): p. 485301.

98. Ji, X., et al., *A theoretical model for metal–graphene contact resistance using a DFT–NEGF method.* Physical Chemistry Chemical Physics, 2013. **15**(41): p. 17883-17886.

99. Janas, D. and K.K. Koziol, *Carbon nanotube fibers and films: synthesis, applications and perspectives of the direct-spinning method.* Nanoscale, 2016. **8**(47): p. 19475-19490.

100. Lekawa-Raus, A., et al., *Electrical Properties of Carbon Nanotube Based Fibers and Their Future Use in Electrical Wiring.* Advanced Functional Materials, 2014. **24**(24): p. 3661-3682.

101. Janas, D., A.C. Vilatela, and K. Koziol, *Performance of carbon nanotube wires in extreme conditions.* Carbon, 2013. **62**: p. 438-446.

102. Zhang, S.L., et al., *Carbon-Nanotube-Based Electrical Conductors: Fabrication, Optimization, and Applications.* Advanced Electronic Materials, 2019. **5**(6).

103. Smith, J.A. and K.S. Kappagantula, *Electrical Performance of Copper-Graphene Nano-Alloys*. 2019, Russ College of Engineering and Technology of Ohio University.

104. Gong, C., et al., *Metal–Graphene–Metal Sandwich Contacts for Enhanced Interface Bonding and Work Function Control.* ACS Nano, 2012. **6**(6): p. 5381–5387.

105. Fuchs, F., et al., *Interaction between carbon nanotubes and metals: Electronic properties, stability, and sensing.* Microelectronic Engineering, 2015. **137**: p. 124-129.

106. Zhang, X., et al., *Achieving high strength and high ductility in metal matrix composites reinforced with a discontinuous three-dimensional graphene-like network.* Nanoscale, 2017. **9**(33): p. 11929-11938.

107. Varol, T. and A. Canakci, *Microstructure, electrical conductivity and hardness of multilayer graphene/copper nanocomposites synthesized by flake powder metallurgy.* Metals and materials international, 2015. **21**(4): p. 704-712.

108. Ponraj, N.V., et al., *Effect of milling on dispersion of graphene nanosheet reinforcement in different morphology copper powder matrix.* Surfaces and Interfaces, 2017. **9**: p. 260-265.

109. Chu, K., et al., *Largely enhanced thermal conductivity of graphene/copper composites with highly aligned graphene network.* Carbon, 2018. **127**: p. 102-112.

110. Cui, Y., et al., *Effect of ball milling on the defeat of few-layer graphene and properties of copper matrix composites.* Acta Metallurgica Sinica (English Letters), 2014. **27**(5): p. 937-943.

111. Jagannadham, K., *Electrical conductivity of copper–graphene composite films synthesized by electrochemical deposition with exfoliated graphene platelets.* Journal of Vacuum Science & Technology B, Nanotechnology and Microelectronics: Materials, Processing, Measurement, and Phenomena, 2012. **30**(3): p. 03D109.

112. Jagannadham, K., *Volume fraction of graphene platelets in copper-graphene composites.* Metallurgical and Materials Transactions A, 2013. **44**(1): p. 552-559.

113. Yin, S., et al., *Novel cold spray for fabricating graphene-reinforced metal matrix composites.* Materials Letters, 2017. **196**: p. 172-175.

114. Yang, K., et al., *Anisotropic thermal conductivity and associated heat transport mechanism in roll-to-roll graphene reinforced copper matrix composites.* Acta Materialia, 2020. **197**: p. 342-354.

115. Jiang, Y., et al., *Reaction-free interface promoting strength-ductility balance in graphene nanosheet/Al composites.* Carbon, 2020. **158**: p. 449-455.

116. Chen, Y., et al., *Fabrication of three-dimensional graphene/Cu composite by in-situ CVD and its strengthening mechanism.* Journal of Alloys and Compounds, 2016. **688**: p. 69-76.

117. Koltsova, T.S., et al., *New hybrid copper composite materials based on carbon nanostructures.* Journal of Materials Science and Engineering B, 2012. **2**(4): p. 240-246.

118. Chen, Y., et al., *Fabrication of in-situ grown graphene reinforced Cu matrix composites.* Scientific reports, 2016. **6**(1): p. 1-9.

119. Dong, L., et al., *Microstructure and properties characterization of tungsten–copper composite materials doped with graphene.* Journal of Alloys and Compounds, 2017. **695**: p. 1637-1646.

120. Cho, J.H., et al., *Controlling the number of layers in graphene using the growth pressure.* Nanotechnology, 2019. **30**(23): p. 235602.

121. He, C., et al., *An approach to obtaining homogeneously dispersed carbon nanotubes in Al powders for preparing reinforced Al-matrix composites.* Advanced Materials, 2007. **19**(8): p. 1128-1132.

122. Kwon, H., et al., *Combination of hot extrusion and spark plasma sintering for producing carbon nanotube reinforced aluminum matrix composites.* Carbon, 2009. **47**(3): p. 570-577.

123. Hashim, J., L. Looney, and M. Hashmi, *Metal matrix composites: production by the stir casting method.* Journal of materials processing technology, 1999. **92**: p. 1-7.

124. Laha, T., et al., *Synthesis and characterization of plasma spray formed carbon nanotube reinforced aluminum composite.* Materials Science and Engineering: A, 2004. **381**(1-2): p. 249-258.

125. López, G. and E. Mittemeijer, *The solubility of C in solid Cu.* Scripta Materialia, 2004. **51**(1): p. 1-5.

126. Lander, J., H. Kern, and A. Beach, *Solubility and diffusion coefficient of carbon in nickel: reaction rates of nickel-carbon alloys with barium oxide.* Journal of Applied Physics, 1952. **23**(12): p. 1305-1309.

127. Degroh, H.C. and U.B. Balachandran, *Conductivity of a Copper-Carbon Covetic Composite.* 2018.

128. Bakir, M. and I. Jasiuk, *Novel metal-carbon nanomaterials: a review on covetics.* Adv. Mater. Lett, 2017. **8**(884): p. 10.5185.

129. Nilufar, S., S. Siddiqi, and I. Jasiuk. *Multi-scale characterization of novel aluminum-carbon nanocomposites*. in *Materials Science and Technology Conference and Exhibition 2012, MS and T 2012*. 2012.

130. Salamanca-Riba, L., et al., *A new type of carbon nanostructure formed within a metal-matrix*. 2012, MARYLAND UNIV COLLEGE PARK.

131. Brown, L., et al., *Physical and mechanical characterization of a nanocarbon infused aluminum-matrix composite.* Materials Performance and Characterization, 2014. **3**(1): p. 65-80.

132. Jasiuk, I., et al. *Novel aluminum-carbon materials*. in *Nanotechnology 2013: Advanced Materials, CNTs, Particles, Films and Composites-2013 NSTI Nanotechnology Conference and Expo, NSTI-Nanotech 2013*. 2013.

133. Balachandran, U., et al., *Nanocarbon-Infused Metals: A New Class of Covetic Materials for Energy Applications.* Advances in Materials Science for Environmental and Energy Technologies VI: Ceramic Transactions, 2017. **262**: p. 205-218.

134. Jaim, H.I., et al., *Sp2 carbon embedded in Al-6061 and Al-7075 alloys in the form of crystalline graphene nanoribbons.* Carbon, 2016. **107**: p. 56-66.

135. Kareem, M.Q., A.H. Jasim, and N.A.-A. Hamza, *Fabrication of aluminium covetic casts under different voltages and amperages of direct current.* Open Engineering, 2020. **10**(1): p. 1-8.

136. Jaim, H.I., D.P. Cole, and L.G. Salamanca-Riba, *Characterization of carbon nanostructures in Al and Ag covetic alloys.* Carbon, 2017. **111**: p. 309-321.

137. Ge, X., et al., *Electrical and structural characterization of nano-carbon–aluminum composites fabricated by electro-charging-assisted process.* Carbon, 2021. **173**: p. 115-125.

138. Knych, T., et al., *Fabrication and cold drawing of copper covetic nanostructured carbon composites.* Archives of metallurgy and materials, 2014. **59**.

139. Yang, Y.F. and M. Qian, *Spark plasma sintering and hot pressing of titanium and titanium alloys*, in *Titanium powder metallurgy*. 2015, Elsevier. p. 219-235.